The Enigmatic Thirteen Micron Feature

A Thesis
presented to
the Faculty of the Graduate School
University of Missouri-Columbia

In Partial Fulfillment
Of the Requirements for the Degree
Master in Science

---

by

Nelson de Queiroz e Souza

Dr. Angela K. Speck, Thesis Advisor

May 2013

The undersigned, appointed by the dean of the Graduate School, have examined the thesis entitled

THE ENIGMATIC THIRTEEN MICRON FEATURE

Presented by Nelson de Queiroz e DeSouza,
a candidate for the degree of Master of Science,
and hereby certify that, in their opinion, it is worthy of acceptance.

Dr. Angela K. Speck, Professor, Director of Astronomy, Dept. of Physics and Astronomy

---

Dr. Linda Godwin, Professor, Dept. of Physics and Astronomy

Dr. Scott D. Kovaleski, Associate Professor, Dept. of Electrical and Computer Engineering

ACKNOWLEDGMENTS

I would like to thank my father and mother whose support throughout my life has been invaluable. My brothers, Thiago and Thomaz, have always kept me grounded. They have given me someone to compete with, resulting in me excelling myself. I would like to thank my fiancé, Brittanny, who has kept me working and on track. As always, I would like to thank my friends who always showed me support.

Certainly none of this would be possible without the support and mentoring of Dr. Angela Speck. I am forever indebted to her for her assistance with my research, advice in my career, and her support throughout these last few years at all times of the day.

Thank you to all of you.

Contents

List of Figures

List of Tables

ABSTRACT

Low and intermediate mass stars (0.8–8 solar masses) will eventually evolve into Asymptotic Giant Branch (AGB) stars and pulsate out their atmosphere into the space around them. That ejected material will eventually cool and form dust. Understanding the nature and formation of cosmic dust is crucial to understanding the Universe. Evolved intermediate mass stars (i.e. AGB stars) are major contributors of dust to the cosmos. Dust around AGB stars are studied by means of infrared spectroscopy from which we observe several interesting spectral features. The observed AGB star spectra have been classified according to their shapes and wavelength positions of the dust features. Alongside the main spectral features around 8-12μm, there is an enigmatic 13μm feature that appears in about half the oxygen-rich AGB stars. The carrier of this feature has not yet been unequivocally identified but has been attributed to various dust species, including corundum (crystalline Al_2O_3), spinel ($MgAl_2O_4$), and silica (SiO_2). While there have been several attempts to determine the cause of this 13μm feature, previous studies have been somewhat contradictory. In order to investigate the origin and characteristics of this spectral feature we observe variations in the 13μm feature over varying stellar parameters. We have also acquired spatially resolved spectroscopic observations of nearby O-rich AGB stars using Michelle on Gemini North. Here we present data on the 13μm feature strength mapped over space around their respective AGB star. The most popular hypothesis for the carrier of the 13μm feature is not supported by our findings.

Chapter 1

Introduction

Early in the history of the Universe, all matter was in the form of hydrogen and helium. Elements more massive than Helium were formed via nuclear fusion in stars and then are ejected from stars either explosively, in the case of supernovae, or gently over a few hundred thousand years, in the case of lower mass stars such as the Sun. The ejected elements cool and form microscopic solid particles (dust grains). The dust becomes part of the interstellar medium (ISM), from which new stars and their planets form. Evolved intermediate mass stars, such as Asymptotic Giant Branch stars (AGB stars), are major contributors of dust to the cosmos.

Understanding the nature of cosmic dust is crucial to understanding the Universe. To study dust grains we have to observe how they absorb and scatter starlight. When dust grains absorb photons, they heat and thus the dust grains emit radiation according to their temperature and other physical properties (i.e. size, shape, composition and crystal structure). Consequently, we observe cosmic dust in the infrared region of the electromagnetic spectrum.

As infrared (IR) astronomy emerged in the late sixties, the importance of the dust particles made from these heavy elements was revealed. Dust plays an essential role in star formation, and contributes to several interstellar processes such as gas heating and the formation of molecules [Videen and Kocifaj, 2002, Draine, 2003, Swamy, 2005, Krügel, 2008].

In addition, since mass loss from evolved stars is driven by radiation pressure on dust grains, it is intimately linked to the precise nature of the circumstellar

dust [Woitke, 2006b]. Furthermore, dust has been observed at higher redshifts than expected, and understanding this phenomenon is vital to our understanding of the cosmos at large and its evolution [Sloan et al., 2009, Bussmann et al., 2009].

Dust grains behave like blackbodies, but with some modifications. For many (but not all) types of dust there will be deviations from blackbody behavior that allow us to identify physical characteristics of the dust. Alongside other spectral features, half of oxygen-rich AGB stars exhibit a spectral feature at 13μm. The carrier of this enigmatic 13μm feature has not yet been unequivocally identified. Hypothesizes have attributed the feature to a variety of materials include corundum (crystalline Al2O3), spinel ($MgAl_2O_4$), and silica (SiO_2).

The purpose of the work presented in this thesis is to constrain the carrier of the 13μm feature. To this end, we have measured the strength, shape, and position of the feature as observed in the spectra of a carefully chosen sample of O-rich AGB stars. These spectral-feature parameters were then compared with various published stellar parameters such as mass-loss rate, proper motion, radial velocity, and variability period. In this way we aimed to determine whether there are any stellar parameters that would be indicative of the dust-forming environment conducive to the occurrence of the 13μm feature. In addition, for a small sample of stars we have spatially resolved spectra of O-rich AGB star. We have compiled the spectral-feature parameters for the 13μm feature as it varies spatially around its parent star. This also provides a diagnostic for which dust-forming environments are conducive to the occurrence of the 13μm feature.

Chapter 2

Stellar Evolution

2.1 Pre-Stellar Evolution

To understand where dust comes from we must first discuss stellar evolution, or the life cycle of stars. Star formation begins in a large dusty molecular gas cloud that collapses under the influence of gravity. As the cloud collapses, it heats up causing the thermal pressure to increase and counteracts the gravitational pull inwards. However, everything with temperature emits photons, and thus the cloud cools, the thermal pressure decreases, and the force of gravity dominates once again, and the gas cloud continues to collapse.

This process continues as the system tries to reach hydrostatic equilibrium (the exact balance of gravity and pressure). Eventually, the cloud collapses to a point where the internal temperature and density deep inside become great enough that hydrogen nuclei can overcome electrostatic repulsion and fusion occurs (also referred to as hydrogen "burning"; see equation 2.1). This is the point when a star is "born".

$$4^1_1 H \rightarrow^4_2 He + energy \tag{2.1}$$

2.2 Hertzsprung-Russell Diagram

In the early 20th century, Hertzsprung (1905) and Russell (1914) independently discovered several patterns when comparing the absolute magnitudes (or luminosi-

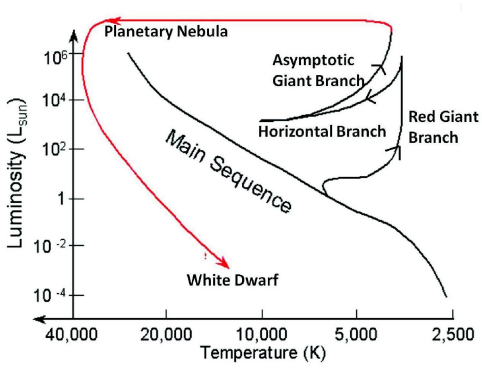

Figure 2.1: Hertzsprung-Russell diagram. The arrows depict the path a solar-mass star takes on the HR diagram as it evolves.

ties) with the surface temperature (or spectral classes) observed for stars. The Hertzsprung-Russell diagram plots luminosity (L_{star}) of a star against its effective surface temperature (T_{eff}). Hertzsprung and Russell recognized that stars are concentrated in certain distinct regions of the L_{star}– T_{eff} space, rather than being distributed at random. It was ultimately discovered that the life cycle of stars, as they evolve, can be plotted on the Hertzsprung-Russell (HR) diagram (figure 2.1).

The life of a star begins on the Main Sequence where it spends most of its life. During this phase the star is fusing hydrogen in its core, producing helium and releasing energy, and thus maintaining hydrostatic equilibrium. The star's position on the main-sequence depends on its initial mass, with the lowest masses to the lower right and the highest masses to the upper left. Stars stay on the Main Sequence phase until the hydrogen in the core is exhausted and fusion stops. At this point the subsequent evolution depends on the initial mass of the star. Low- and intermediate-mass stars (0.8–8 $M_{\odot}$; LIMS) make up 95% of stars and produce the majority of the dust complement for the Galaxy so we will follow stars in this mass range [Kwok, 2004].

Without the thermal pressure, created by the energy released in H-fusion, hydrostatic equilibrium is lost and gravity once again dominates causing the core of the star to collapse further. The core is made of He created during the H-burning of the main-sequence, but the mantle of the star is still mostly hydrogen. The collapsing core drags the inner mantle along which heats up as potential energy is converted to

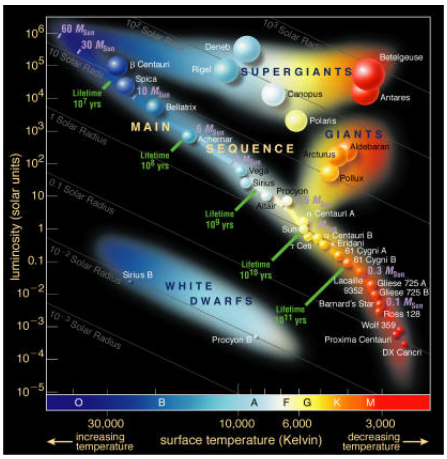

Figure 2.2: The Hertzsprung-Russell diagram. Temperature is plotted on the x-axis, increasing towards the left (customary) as luminosity is plotted on the y-axis [Cain, 2009].

kinetic energy. This heat causes the concentric shell of hydrogen atoms surrounding the dormant helium core to begin fusing. Stars now enter the Red Giant phase. Note that it is now the shell around the core where hydrogen burning is occurring as opposed to in the core, as was the case for main sequence stars.

The rate at which H-fusion proceeds is greater than it had been during the main-sequence, resulting in more energy production and thus there is an increase in the luminosity (L_{star}). The increase in energy flowing into the non-fusing H-gas of the outer mantle of the star causes it to expand hugely which decreases the effective temperature (T_{eff}).

The core of the star continues to collapse because it still is not generating energy to support itself. The path the star now takes depends upon its mass and the percentage of elements other than hydrogen and helium. There are four potential paths these stars can take.

If the star has a mass less than $\sim 0.8 M_{\odot}$, the core will be degenerate helium; i.e., the pressure due to quantum mechanical interactions between electrons dominates over the thermal pressure. Such a low mass star can never overcome this degeneracy and the helium core never ignites.

If the star has a mass between ~ 0.8 and $\sim 4 M_{\odot}$, the core will also be degenerate helium. However, the hydrogen burning in the shell around the core will heat the core. If the stellar mass is less than $\sim 2.5 M_{\odot}$, the helium is ignited so that it begins

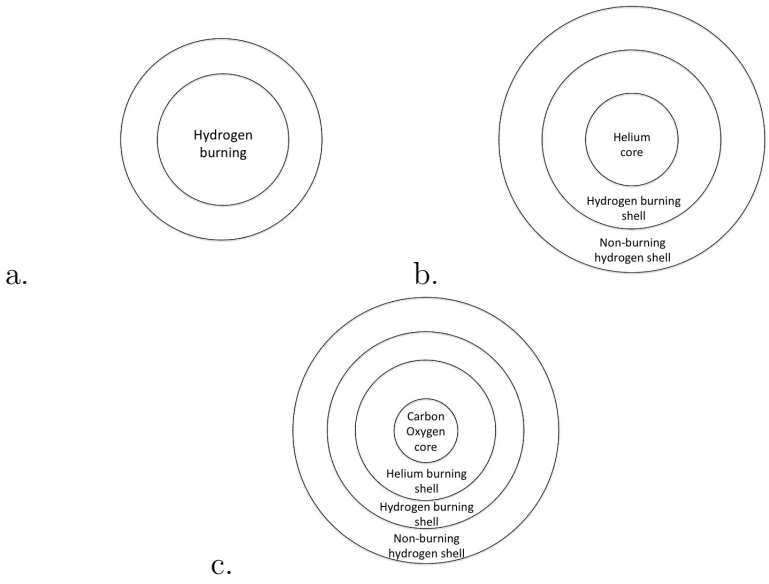

Figure 2.3: A cartoon schematic of the cross-section of low- and intermediate mass stars at different phases of evolution. a. Main Sequence Star. b. Red Giant Star. c. AGB star. Images are not drawn to size.

to fuse without overcoming degeneracy and we get a helium flash. This flash occurs because the degenerate helium core is a good conductor; once fusion starts the energy quickly spreads through the core and induces fusion to start throughout the core almost instantaneously. Hence there is a rapid increase in luminosity at that moment, known as the helium flash.

If the stellar mass is more than $\sim 2.5 M_{\odot}$, sufficient energy is supplied from the hydrogen-burning shell that the core heats up enough to become non-degenerate before the onset of helium fusion. If the star has a mass between ~ 4 and $\sim 8 M_{\odot}$, the core is hot always enough so that it does not become degenerate at all.

The fusion of helium into carbon occurs by the triple-α process (see equation 2.2)

$$3^4_2 He \rightarrow^{12}_6 C + energy \tag{2.2}$$

The star now enters the Horizontal Branch (HB) phase. Just like the main-sequence H-burning, the helium in the core will eventually be exhausted and the core He-burning will cease.

Yet again, hydrostatic equilibrium is lost and the core begins to collapse again. As with the onset of the Red Giant phase, the increase in temperature from the

collapse causes concentric shells surrounding the dormant core to start fusing hydrogen and helium, respectively. The star has now entered the Asymptotic Giant Branch phase (AGB; figure 2.1). The AGB asymptotically approaches the Red Giant Branch (or RGB) and the behavior of the star in the AGB phase mirrors that of the RGB; the rate of fusion is greater than the previous burning, resulting in more energy production; greater luminosity (L_{star}) and an expanded star with a decreasing effective temperature (T_{eff}).

2.3 AGB Stars

AGB stars are very luminous ($L_{star} \sim 10^4 L_\odot$), cool ($T_{star} \sim 3000K$) giant stars ($R_{star} \sim 1AU$). They consists of a degenerate carbon and oxygen core with concentric helium and hydrogen burning shells (see figure 2.3). The energy produced from both shells needs to escape the star and does so through two processes; convection and radiation.

Deep within the AGB star, temperatures can rise sufficiently so that hydrogen is ionized. The ionization of hydrogen causes the opacity of the gas to increase, which means a higher temperature gradient is required for energy to be transported out of the area [Habing and Olofsson, 2004], which would suggest that convection is preferred.

At the same time, the ionization of hydrogen affects the adiabatic temperature gradient so if the gas were to move away from the core adiabatically, it would cool. However, cooling the gas would cause the electrons to recombine with the ionized hydrogen, releasing energy and heating the gas up again [Habing and Olofsson, 2004], which would mean radiation is preferred.

Therefore, the process by which a star releases its energy from burning will depend on the change of temperature compared to the change in pressure. Generally, a star radiates heat closer to the core while convection dominates closer to the surface.

2.3.1 Dredge-up and *s-process* Elements

The helium-burning shells turning on and off causes a thermal pulse which can cause the convection envelopes in the mantle to reach between the hydrogen and helium burning shells. This means the new materials formed by helium-burning will be brought to the surface of the star. This process is called a "dredge-up" and the timescale between dredge-ups is $\sim 10^4$- 10^5 years depending on the initial mass and metallicity[1] of the star. As a result of dredge-ups, elements from deep inside the star can be found in the surface of the star. This includes more than just the aforementioned carbon, oxygen, helium, and hydrogen, because other processes, such as the *s-process*, form other elements in the star. Stars may also have elements that were formed in a previous generation star that died and the elements from that star make up the new star.

All elements more massive than ^{26}Fe are created via neutron capture. This process can happen rapidly (as in supernova explosions) or slowly, which is relevant to AGB stars. In this case, known as the *s-process*, a new nucleus is made via capture of a neutron; if it is not stable it will then decay radioactively prior to capturing another neutron. There are three *s-process* components that produce elements and depend on the neutron flux. The three components are called the weak, main, and strong components. The weak component requires the lowest neutron flux and is responsible for most of the *s-process* with atomic numbers less than 90. The main component requires a larger neutron flux and is responsible for s-isotopes with atomic numbers between 90 and 204. The strong component requires a significantly larger neutron flux and is primarily accountable for the ^{208}Pb production in the solar system.

$$^{13}_{6}C + ^{4}_{2}He \rightarrow ^{16}_{8}O + n \tag{2.3}$$

When carbon interacts with helium, as seen in equation 2.3, a neutron (n) is released. When that neutron is captured by an iron atom, the iron element can undergo β-decay (see equation 2.4) in which the neutron will be converted into a

[1] The relative mass abundance of elements other than hydrogen and helium.

proton. This occurs because the atom is unstable and the reaction will result in an element with a higher atomic number. This process can continue, resulting in atoms of a variety of atomic numbers.

$$^{14}_{6}C \rightarrow ^{14}_{7} N + e^{-} + v_e \tag{2.4}$$

This is significant because when a star pulsates (a process discussed next), the material on the surface of the star is expelled out of the star. Therefore, the material expelled is not just hydrogen and helium, but also the materials brought to the surface in the dredge-up.

2.3.2 Stellar Pulsation and Dust

Beginning in 1595, it has been observed that certain stars vary in luminosity. It has since been determined that this periodic brightening is caused by stellar pulsation. The mechanism for pulsation is believed to be a result of changes in the opacity of the gas of the star with temperature. As the gas expands it cools and its density/pressure decreases. This causes recombination of electrons with atoms, which reduces the opacity further and thus pressure gets so low that the gas collapses under gravity. However, as the gas collapses, its density and temperature increase, becoming more opaque. This causes the energy to "dam up", heating the gas and eventually causing it to expand out again. As the gas expands and the energy is released, the gas cools and the process begins again [Carroll and Ostlie, 2007].

Stellar pulsation combined with low surface gravity leads to the escape of atmospheric gases escaping from their parent stars. Pulsations levitate atmospheric material allowing it to achieve an altitude where cooling temperatures allow molecules to form [Alexander and Ferguson, 1994], followed by formation of microscopic solid particles (dust grains). As a result, AGB stars are surrounded by dusty circumstellar envelopes (figure 2.4).

The exact temperature at which dust forms is unclear, but is expected to be in the range 600-2000K [Speck et al., 2008, Speck et al., 2009, Speck, 2012]. Once dust is formed, radiation pressure becomes very important. As the dust grains are

driven outwards by radiation pressure, they drag along the surrounding molecular gas [Höfner and Dorfi, 1997].

The optical properties of the dust grains affect the transfer of momentum from the stellar radiation and thus mass-loss rate. Optical properties are determined by the mineralogy and size/shape of the dust grains (see chapter 3 for relevant details). Therefore, the precise nature (composition, crystal structure, grain size and shape) of circumstellar dust will affect the evolution of the star through the feedback mechanism of dust-driven stellar winds. Moreover, the detailed nature of the dust will affect any other environments into which dust is injected because the light–solid interaction is modified according to the details of the dust.

2.3.3 Chemistry of AGB Stars

During their ascent of the AGB, the stars evolve chemically, starting with oxygen-rich atmospheres. The helium burning forms ^{12}C deep inside the star. As described in section 2.3.2, dredge-up caused by the convective stellar mantle, brings newly-formed carbon atoms up to the surface of the star. Thus, carbon is injected into the stellar atmosphere.

The stability of the carbon monoxide (CO) molecule in the stellar atmosphere means that the C/O controls the chemistry around the star: whichever element is less abundant will be entirely locked into CO molecules, leaving the more abundant element to control dust and molecule formation. Therefore AGB stars are usually either carbon- (C-) rich or oxygen- (O-) rich. For the O-rich AGB stars C/O can vary from approximately cosmic C/O $\sim$0.4) to just less than unity. Once C/O exceeds unity, all O-atoms are trapped in CO and carbon dominates the chemistry. Carbon-rich stars are beyond the scope of the present work.

Along with carbon, dredge-ups will also bring other elements to the surface (e.g. Zirconium, an *s-process element*). Therefore, dredge-ups will cause C/O to increase, the quantity of available O-atoms to decrease, and the quantity of other materials to increase. Stars in the 2–4$M_\odot$ range become carbon rich while lower mass stars do not generate or dredge up sufficient C atoms. Higher mass stars (>4$M_\odot$) destroy C-atoms in Hot Bottom Burning and turn ^{12}C into ^{14}N in the CNO cycle. This

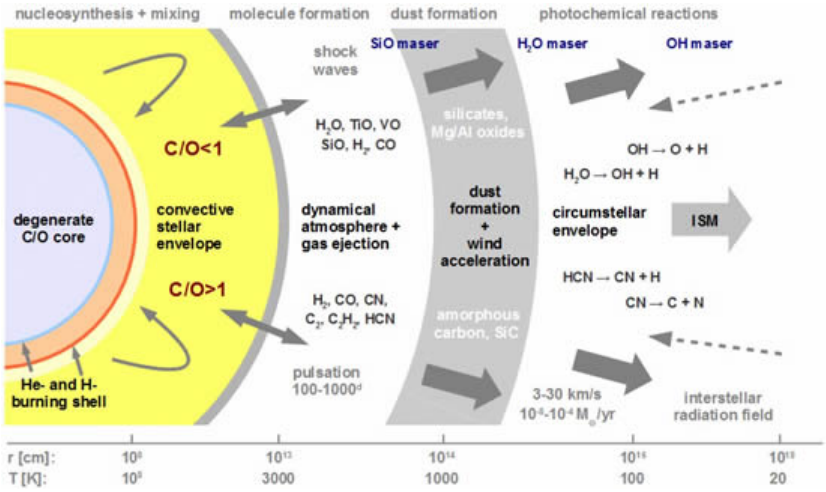

Figure 2.4: A schematic of where dust formation occurs relative to a star [Woitke, 2006a].

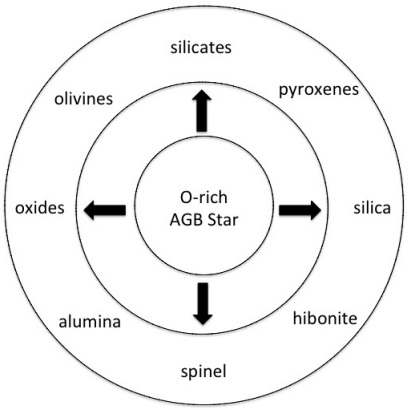

Figure 2.5: Examples of dust that forms in the circumstellar envelope of O-rich AGB stars.

means that the chemistry of a high mass O-rich AGB star is more nitrogen-rich.

It is expected that the dust formation process will follow a dust condensation sequence [Tielens, 1990, Stencel et al., 1990, Gail and Sedlmayr, 1999, Lodders and Fegley Jr, 1999], which describes the order in which various dust species condense from a cooling gas (see figure 2.6). For O-rich stars the resulting dust species will be O-rich, e.g. magnesium-iron (Mg-Fe) silicates and oxide and calcium-aluminium (Ca-Al) compounds. In contrast, when C/O ¿ 1, the excess C leads to the formation of C-rich dust species like graphite/amorphous carbon and carbides as well as sulfides.

Now that we have discussed stellar evolution and how dust forms around AGB

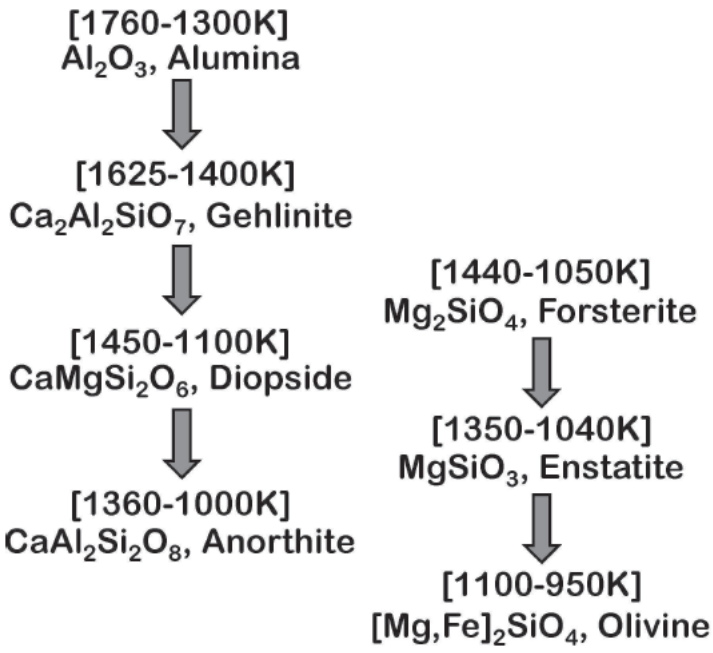

Figure 2.6: The predicted dust condensation sequence for O-rich stars [Tielens, 1990].

stars, we will discuss how we can study that dust. Chapter 3 focuses on how spectra from the dust are analyzed and what it can tell us about the dust.

Chapter 3

Studying Dust in Space

In order to study stars and the dust around them, we look at the light spectrum from the star and dust. Therefore, we must know how the dust grains interact with light.

Light from an AGB star is absorbed by its circumstellar dust and reemitted, usually in the infrared wavelengths (IR; 750nm to 1mm). The circumstellar dust grains around AGB stars are studied by looking at the IR wavelengths spectral features. The composition, lattice structure, size, shape, and mass fraction of the dust grains as well as the temperature and density distribution of the dust within the circumstellar envelope all affect the IR features.

3.1 Optical Properties of Solids

Any object with a temperature above 0K will emit light at all wavelengths. A blackbody is an object absorbs all of the light energy that hits it, without reflecting any of the light, and then re-emits that energy. The re-emission, or radiation, will be a spectrum dependent on the nature of the body (i.e. its structure, composition, temperature). The radiation from a blackbody is a continuous spectrum as given by the Planck function (see equation 3.1) [Carroll and Ostlie, 2007].

$$B_\lambda(T) = \frac{2hc^2/\lambda^5}{e^{hc/\lambda kT} - 1} \tag{3.1}$$

a.

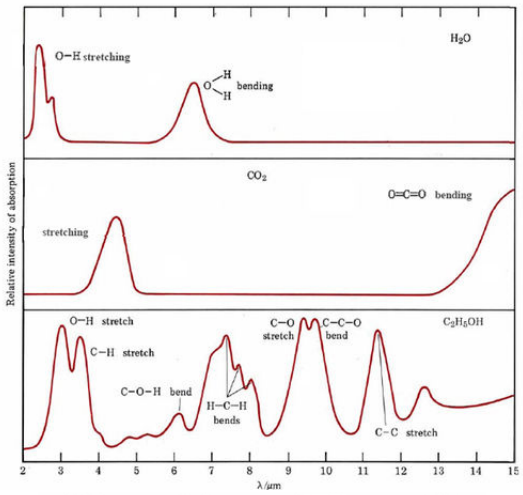

b.

Bond	λ/μm	Bond	λ/μm
—C—H	3.4–3.5	—C—C—	6.6–16.7
=C—H	3.2–3.3	C=C	5.9–6.2
≡C—H	3.0	—C≡C—	4.4–4.8
—O—H	2.5–2.8	—C—O—	7.7–10.0
—O—H*	2.9–3.1		
—N—H	2.8–3.0	C=O	5.7–5.9
		—C≡N	4.3–5.0

Figure 3.1: a. The emission spectra of H_2O, CO_2, and C_2H_5OH gasses. b. A sample of different bonds and the respective wavelength at which the photon would be emitted [Moore, 1978].

We can approximate stars and planets to be blackbodies, but dust grains are not perfect blackbodies. When a dust particle is placed in a beam of light, it absorbs and scatters parts of the light. The amount of the light that is scattered and absorbed is called extinction. The amount and wavelength of extinction depends on the nature of the dust grains (i.e. composition, lattice structure, grain size, grain shape, temperature, and mass fraction).

When a bond bends or stretches, energy can be emitted as a photon. Figure 3.1a is a sample of different molecules' spectra. It shows how the bending and stretching of different bonds can result in the emission of a photon at a particular wavelength. Different molecules have unique structures and bonds between their atoms, which means that the energy emitted will be in an unique set of wavelengths (e.g. figure 3.1b).

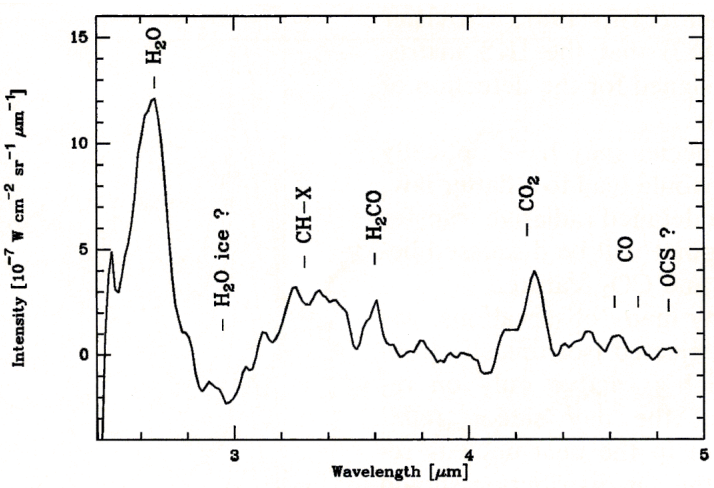

Figure 3.2: An example of IR emission and absorption features of several molecules together [Cline, 2010].

Therefore, by studying the light (energy) that is emitted from a mixture, we can attempt to determine what compounds are in that mixture. The molecule that emits at a particular wavelength is called the "carrier" while the wavelength emitted is seen as a "feature" in a graph of intensity versus wavelength. The emissions spectra can become more complicated as more molecules are present in a sample (e.g. figure 3.2), so let us discuss how we analyze spectra.

3.2 Analysis

In this thesis, we are interested in the dust that surrounds AGB stars. Therefore, we have to look at the spectrum produced by the star and its circumstellar dust. This spectrum can be represented by a sum of the fluxes contributing to it:

$$F_{total}(\lambda) = F_{star}(\lambda) + F_{dust}(\lambda) \tag{3.2}$$

As stated in section 3.1, a star is essentially a blackbody with a temperature T_{star} whereas the dust is made up of contributions from each dust grain of difference sizes, shapes, compositions and crystal structures. The flux from an individual dust grain is a product of the Planck function (i.e. equation 3.1) for the temperature of the individual dust grain and an extinction efficiency factor, $Q_{\lambda,}$ for a grain of that

size, shape, composition and crystal structure.

Therefore, the first step in analyzing spectra is to manually fit a continuum to each spectrum. However, this process is complicated by the presence of strong molecular bands throughout the spectral range of the observations. When unrecognized, these molecular bands can lead to misinterpretation of the continuum level, which gives rise to spectral artifacts in the guise of apparent emission features [Thompson et al., 2006, Speck et al., 2006]. Strong molecular absorptions and emissions in the spectra can obscure the true level of the continuum. In particular, automatic fitting routines and χ^2 analyses of the quality of fits are precluded by the problem of limited true continuum in these spectra.

There are various options for removing the continuum from the spectra and obtaining just the dust emission and absorption contributions. The question becomes which method is most valid for our situation.

3.2.1 Continuum subtracted or divided

The first method is to consider a simplified case in which the spectrum, $F_{total}(\lambda)$, can be interpreted as a product of the underlying continuum and an extinction efficiency factor, $Q_{\lambda,}$ for the entire spectrum,

$$F_{total}() = C \times Q_{\lambda} \times B_{\lambda}(T) \tag{3.3}$$

where $B_{\lambda}(T)$ is the Planck function (see equation 3.1) for a black body of temperature T, Q_{λ} is a composite value including contributions from all dust grains of various sizes, shapes, crystallinities and compositions, and C a scale factor that depends on the number of dust particles, their geometric cross section and the distance to the star.

Using a simple continuum-divided spectrum assumes the type of spectrum described by equation 3.3. Dividing the entire spectrum by the fitted underlying continuum leaves only the absorption and emission of the dust (assuming all dust species have the same blackbody temperature). The continuum-divided spectrum is effectively an optical depth spectrum, which is equivalent to an extinction effi-

ciency for some sort of composite grains that represents all the grains present. Using this technique implicitly assumes that the silicate grains[1] are the dominant cause of wavelength dependent changes to the optical depth, and fails to account for different sizes, shapes and/or temperatures within the silicate grain population.

The second method is where a continuum is subtracted from the spectrum (see e.g. [Niyogi et al., 2011], and references therein). In this case, the continuum is taken to be due to the flux of the star or to metallic iron grains (which do not have diagnostic mid-IR features and thus Q is a power law). This implies that the continuum-subtracted spectrum is due to silicates, but neglects the fact that silicates will also contribute to the continuum.

Both scenarios are oversimplifications of the true situations and it is difficult to know which approach is most appropriate. In reality the spectrum should be represented by:

$$F_\lambda = F_{star} + \sum_{i=1,j=1}^{n,m} C_j \times Q_{\lambda,j} \times B_{\lambda,i}(T_i) \tag{3.4}$$

where each B_i represents a single dust (or stellar) temperature black body (of which there are n in total), each Q_j represents the extinction efficiency for a single grain type as defined by its size, shape, composition and crystal structure, and each C_j represents the scale factor for a single grain type (of which there are m in total); i.e. at each given wavelength the emission from the individual dust species is simply added to give the total emission at that wavelength.

However, such a complex analysis is not feasible and approximations and simplifications must be made. Reel et. al. (2013) (in prep) show, through an analysis of carbon-rich AGB star, V Cyg, that either scenario is valid for optically thin shells[2] and actually return the same results. Since we are dealing with optically thin shells, either method will be valid for our spectral analysis.

Reel et. al. (2013) also determined that the sum of several individual blackbodies can be approximated with a single blackbody fit (see figure 3.3). It is important to

[1] Recall that the dust is dominated by magnesium-silicates according to dust condensation models (see section 2.3.3).

[2] i.e. a significant fraction of starlight traverses the circumstellar dust unscathed.

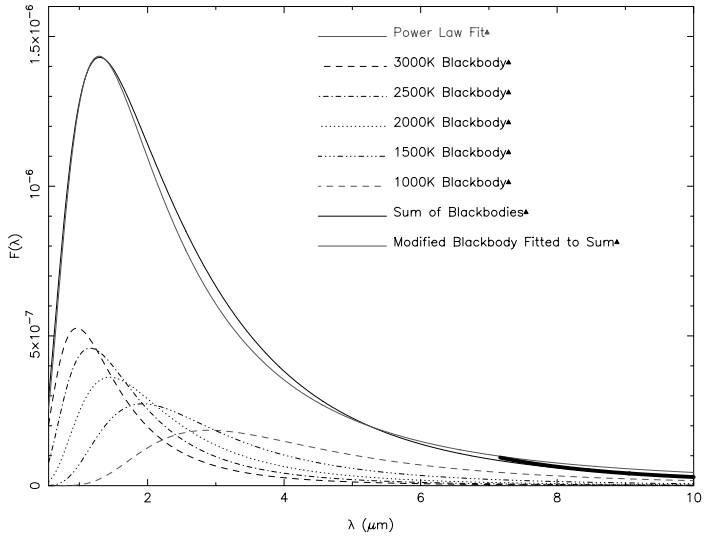

Figure 3.3: A demonstration of the effect of summing blackbodies on the continuum-fitting processing. The thicker line from 7-13μm is a power law fit as an example of what was done in this thesis to remove the continuum. x-axis in wavelength in μm; y-axis is flux density in arbitrary units (Reel et. al. 2013 (in prep)).

note that in the Reel et. al. (2013) used a blackbody to fit the continuum, but in this paper the spectra were fit using a simple a power law. As per the Rayleigh-Jeans law, a blackbody can be approximated using a power law provided that the area being fit is significantly far away from the blackbody peak. This is true of the data analyzed in this thesis and is shown in figure 3.3 as the thicker line from 7-13μm.

3.3 Classification of silicate spectral features

Once the continuum is removed from the spectra, classifications can be made in an attempt to group together stars that exhibit similar features and feature strengths (see e.g. [Little-Marenin and Little, 1988, Speck et al., 2000, Sloan and Price, 1995]). One such classification is the silicate emission (SE) classification of oxygen-rich stars developed by Sloan and Price (1995). The classification is intended to follow the progression of the silicate feature as it progresses from a narrow to a broad feature. This was done by comparing the flux at 10, 11, and 12μm. When plotting F_{10}/F_{11} versus F_{10}/F_{12}, they discovered that most stars fell near an empirical power law,

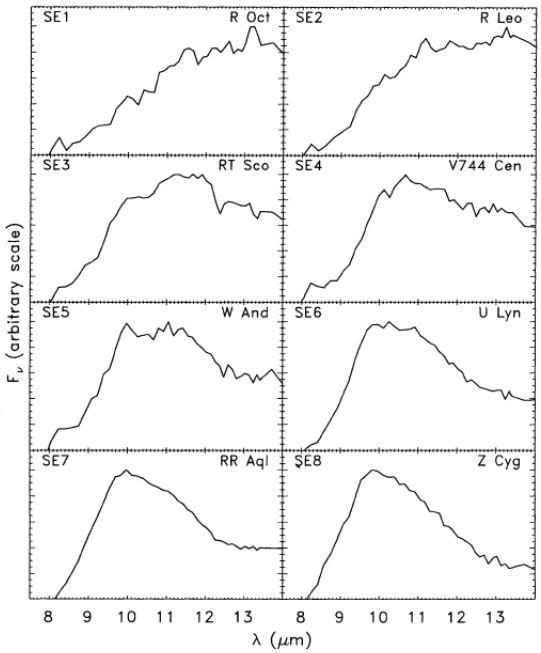

Figure 3.4: A sample of the progression of the silicate feature through the SE classes.

$$F_{10}/F_{12} = 1.32(F_{10}/F_{11})^{1.77} \tag{3.5}$$

They could then categorize the stars by using the ratio of flux at 11 and 12μm in equation 3.6, where the truncated n is the SE class the star would belong to.

$$n = 10(F_{11}/F_{12}) - 7.5 \tag{3.6}$$

There is a particular spectral feature around 13μm (see figure 3.5) that is observed in half of oxygen-rich AGB stars. In the process of developing the SE classification, Sloan and Price (1995) found that the feature was observed in all SE classes and thus treated the feature independently of their classification. The carrier of the feature is currently undetermined, but several hypotheses have been presented (see chapter 5). This feature is the focus of this thesis. In an effort to narrow the possibilities of carriers of the 13μm feature, we present data on the lack of correlations between the 13μm and different stellar parameters such as radial velocity, and galactic coordinates. We will also present data on how the 13μm feature varies spatially around the central star.

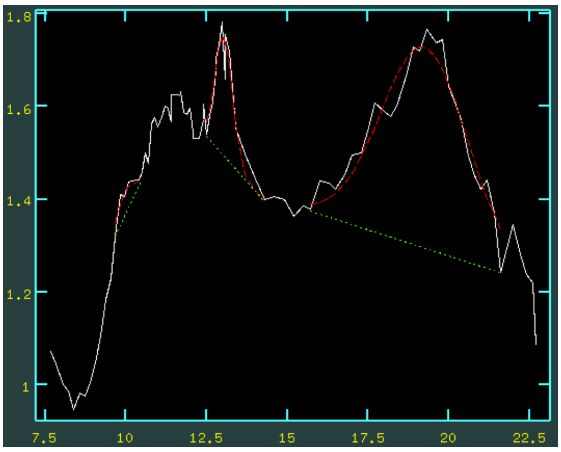

Figure 3.5: A spectra depicting the 10, 13, and 19μm features.

Chapter 4

The Thirteen Micron Feature

In this chapter we discuss what is known about the 13μm feature and what are the current competing hypotheses for its cause.

4.1 Observations of the 13μm feature

The 13μm feature is virtually never observed in supergiant spectra and is observed in half of the O-rich AGB stars. Of those O-rich stars, it is found most often in spectra with both a broad feature (extending from 8.5 to 12μm) and the classic silicate feature. It is sometimes found in spectra with just the classic silicate feature and rarely found in spectra with just the broad feature.

It has also been found that 75-90% of semiregular variable stars exhibit the 13μm feature in their spectra [Sloan et al., 1996] while only 20-25% of Mira spectra have the feature. So let us begin by looking at the difference between Miras and semiregular variables.

4.1.1 Miras and Semiregular Variables

Miras and semiregular variables both belong to a subset of stars called variable stars. Variable stars are stars whose apparent magnitude fluctuates over time. Miras have a regular pulsation with a period longer than 60 days and a large amplitude ($\geq$ 2.5magnitudes in the visible wavelengths). Semiregular variables (SR) are less regular in their pulsation and have a smaller amplitude ($\leq$ 2.5magnitudes in the visible

wavelength). Semiregular variables can be further separated into four subgroups (SRa, SRb, SRc, and SRd), which are defined by how regular or irregular their period is, how luminous they are, or their color or spectral type.

The relationship between Miras and semiregular variables has often been hypothesized. One hypothesis was the semiregulars are less evolved than Miras (e.g. [Feast and Whitelock, 1987]). However, their IR spectral features are similar and both cover the full range of classification. This would suggest that the evolution is not observed in the dust.

Another set of hypotheses is that semiregulars and Miras form a continuous sequence. That is to say that either Miras are the progenitors of semiregulars [Habing, 1996] or that semiregulars are the progenitors or Miras [Kerschbaum and Hron, 1992]. However, an examination of the amplitudes of variability and their stabilities suggests that Miras and SRs are distinct from one another [Mattei et al., 1997]. This contradicts the claim that Miras and semiregulars form a continuous sequence, but whether one is the progenitor of the other is still uncertain.

Moreover, it is hypothesized that the progression from a broad to a narrow silicate feature (see section 3.3) is evolutionary. If that is true, then Miras' spectra progress as expected while semiregulars have no trend [Hron et al., 1997].

Finally, it has been hypothesized that stars alternate between being Miras and semiregulars [Kerschbaum and Hron, 1992]. Therefore, the star would have periods of regular pulsation with large amplitudes and periods of more irregular pulsation with a smaller amplitude. Since the 13μm is observe more often in semiregulars, perhaps the carrier can only form in that environment. It is then quickly destroyed or coated by the lower condensation temperature material in the environment of Miras. The Miras that do exhibit the 13μm feature could be explained as stars who have not yet destroyed or coated all of the 13μm feature carrier.

Justtanont et al. (1998) found a correlation between CO_2 emission lines and the 13μm feature. This suggests that the carrier of the 13μm feature and CO_2 formation occurs in similar environments. Therefore, the 13μm feature carrier would form in warm gas layers close to stars with low mass-loss rates, such as the low density dust shells around semiregular variables. The higher mass-loss rates preclude the

formation or the excitation of CO_2 and the same would be true for the 13μm feature carrier.

Whatever the cause/carrier of the 13μm feature its presence must be able to be explained by the difference between SR variables and Miras. Several potential carrier minerals have been put forward which are discussed below.

4.2 Corundum

The 13μm feature was hypothesized to be alumina (Al_2O_3) dust grains [Hackwell, 1972, Vardya et al., 1986, Onaka et al., 1989, Little-Marenin and Little, 1990, Glaccum, 1995]. Alumina is found in several different forms though only one is naturally found on earth; corundum (α-Al_2O_3).

The Al-O bond emissions could explain the 13μm and condensation models [Salpeter, 1974, Sedlmayr, 1989, Tielens, 1990, Kozasa and Sogawa, 1997, Kozasa and Sogawa, 1998] suggest that alumina should be the first dust type to condense around O-rich AGB stars. However, alumina could then act as a nucleation seed where silicates could form a mantle [Vardya et al., 1986, Onaka et al., 1989, Tielens, 1990, Kozasa and Sogawa, 1997, Kozasa and Sogawa, 1998]. It was then suggested that the emission from the Al-O bond dominates initially, but then the emission from the Si-O bond, which is more abundant, dominates.

Also, if the 13μm is emitted by the first dust type to condensate, then we would expect the 13μm feature to be often found in spectra with the broad feature. However, the 13μm feature is more common to spectra exhibiting both the broad and silicate features.

Corundum (α-Al_2O_3) remains a viable candidate, with only small amounts (∼1% compared to warm silicates) needed to produce the 13μm feature [DePew et al., 2006]. However, along with the 13μm feature, corundum should cause a weaker feature at 20.5μm, which is not observed but is predicted to be difficult to observe [Glaccum, 1995, Begemann et al., 1997]. Models that show at low relative abundances of corundum (less than ∼25%), the 20.5μm feature is hidden by silicate features [DePew et al., 2006].

The optical depth of the dust is critical in determining if the features of corundum are observed. The 13μm of corundum is visible in low optical depths, but when the optical depth increases the feature goes to absorption. The exact optical depth at which this occurs depends on the relative abundance of corundum.

However, since the feature has never been observed in absorption, the optical depth must be restricted to the optical depth observed in stars with the 13μm feature.

The 13μm feature of corundum is not observed in high optical depth oxygen-rich stars [Maldoni et al., 2005]. This suggests that, if corundum is the carrier of the 13μm feature, higher density dust stops its formation [DePew et al., 2006] or causes it to be rapidly coated in silicate to hide its features (c.f. Chan & Kwok and coating of SiC by carbon in C-rich AGB stars).

4.3 Spinel

According to condensation models (see figure 2.6) when corundum cools, it reacts with gaseous SiO, Mg, and Al to produce spinel ($MgAl_2O_4$). Spinel was one leading candidate as carrier of the 13μm feature, but it exhibits secondary features at 17μm [DePew et al., 2006], which are not observed in stellar spectra [Sloan et al., 2003, Heras and Hony, 2005]. We will not consider spinel further.

4.4 Silica

Another potential carrier for the 13μm feature is silica [Speck et al., 2000]. This is a controversial candidate because it is not included in the classic condensation sequences for O-rich AGB stars. In particular, Lodders and Fegley Jr (1999) described circumstellar silica (SiO_2) as "mythical" because equilibrium condensation calculations show that Si forms Mg-rich silicates (and not SiO_2). However, silica may originate during rapid cooling under non-equilibrium conditions in stars with low Mg/Si ratios [Gail and Sedlmayr, 1999]. Evidence pointing towards non-equilibrium condensation of amorphous silica aggregates also comes from labora-

tory experiments [Rietmeijer et al., 1999], and models of kinetically condensing systems [Nagahara and Ozawa, 2009]. The latter study suggests that SiO_2 may form in circumstellar outfows because condensation of metallic Fe onto forsterite prevents the formation of enstatite. Thus, the silica stardust grains found in this and other studies may have formed through kinetically driven reactions in stellar environments.

Laboratory extinction spectra of the three main polytypes of crystalline SiO_2, quartz, tridymite and cristobalite, as well as amorphous silicon dioxide and silica glass exhibit the 13μm feature [Speck et al., 2000, DePew et al., 2006], although detailed modeling remains problematic [DePew et al., 2006]. However, arguments have also been raised against SiO_2 as the carrier of the 13μm feature, including opacity issues leading to reduced emission at the IR wavelengths, and the absence of a correlation between the 13μm and 10μm silicate features in all stellar spectra [Fabian et al., 2001].

Nevertheless, if silica is indeed a product of non-equilibrium condensation, it may be a feasible carrier of this spectral feature in Semi Regular variable stars. These stars have lower mass loss rates than Mira variable stars, leading to a lower density at the dust-forming radius (Ivezic and Knapp, 1999). Non-equilibrium conditions prevail at these lower densities, with the result that silica is less likely to react with other circumstellar species (e.g., MgO) to form magnesium silicates and, thus, may survive as SiO_2.

In the next two chapters we will see two separate investigations of O-rich AGB stars aimed at determining the carrier of the 13μm feature.

Chapter 5

Variations in the Thirteen Micron Feature in a Sample of AGB Stars

Here we present data and parameters for a large sample of oxygen-rich AGB stars and determine whether the strength of the 13μm feature is correlated with any of these stellar parameters such as proper motion, radial velocity, and period.

5.1 Sample Selection

Each of the prevalent hypotheses for the carrier of 13μm feature preferentially forms in different dust conditions (see chapter 4). The conditions of the dust around stars is not known, but can be inferred from different stellar parameters such as mass-loss rate. Therefore, we sought correlations between the strength of the 13μm features and the stellar parameters of the star.

In order to test if the presence of the 13μm feature had any correlation with stellar parameters, we began by selecting a small sample. The criteria for the sample were AGB stars for which IRAS LRS data was available and that were determined to have a 13μm feature in [Sloan and Price, 1995]. The reason for this second criterion is that Sloan and Price (1995) had a rigorous test for determining the presence of a 13μm feature. They fit polynomials to the spectrum from 10.66–12.59μm and again from 13.72–15.18μm. Excess emission above the polynomial from 12.70-13.41μm was defined as 13μm emission. The spectra were deemed to have a 13μm feature only if

IRAS PSC Name	Source	SE Class	Variable Type	
20038-2722	V1943 Sgr	3	Lb	Pulsating Variable
02427-5430	W Hor	3	SRb	Semi-Regular Pulsating
14219+2555	RX Boo	3	SRb	Semi-Regular Pulsating
16387-2700	AX Sco	3	SRb	Semi-Regular Pulsating
19194+1734	T Sge	3	SRb	Semi-Regular Pulsating
20079-0146	V584 Aql	3	Lb	Pulsating Variable
17123+1107	V438 Oph	3	SRb	Semi-Regular Pulsating
13022-7650	DL Cha	3	SRb	Semi-Regular Pulsating
13303-0656	S Vir	3	M	Mira Cet
13462-2807	W Hya	3	SRa	Semi-Regular Pulsating
02427-5430	W Hor	3	SRb	Semi-Regular Pulsating
14219+2555	RX Boo	3	SRb	Semi-Regular Pulsating
16387-2700	AX Sco	3	SRb	Semi-Regular Pulsating
17123+1107	V438 Oph	3	SRb	Semi-Regular Pulsating
19194+1734	T Sge	3	SRb	Semi-Regular Pulsating
20038-2722	V1943 Sgr	3	Lb	Pulsating Variable
20079-0146	V584 Aql	3	Lb	Pulsating Variable
06551+0322	AZ Mon	3		Mira Cet
10580-1803	R Crt	3	SRb	Semi-Regular Pulsating
04361-6210	R Dor	7	SRb	Semi-Regular Pulsating
04265+5718	RV Cam	6	SRb	Semi-Regular Pulsating
12046-0629	RW Vir	3	SRb	Pulsating Variable
20502+4709	RZ Cyg	3	Sra	Semi-Regular Pulsating
22035+3506	SV Peg	3	SRb	Semi-Regular Pulsating
00192-2020	T Cet	1	SRc	Semi-Regular Pulsating
04020-1551	V Eri	3		Semi-Regular Pulsating
02469+5646	W Per	5	SRc	Semi-Regular Pulsating

Table 5.1: A list of the sample stars used in the stellar parameter study.

"1) both polynomials gave a 4σ detection, and 2) in one of the two fits, the 13μm emission is stronger than 5% of the continuum" [Sloan and Price, 1995].

In order to limit our sample size, and to not introduce a possible confounding variable, we selected only SE3 class stars [Sloan and Price, 1995], (see also chapter 3). The sample size was later increased to include stars from other SE classes, but the sample is still dominated by SE3 class stars. The sample stars are listed in table 5.1.

Spectral data was obtained from IRAS LRS. As discussed in chapter 3, there is some debate on whether a continuum should be divided out or subtracted from an observed spectrum. In order to further validate the fact that subtracting and dividing the fitted power-law continuum will yield the same results (see section 3.2.1) we used both approaches and compared the resulting measurements of the spectral feature parameters.

The 13μm spectral feature parameters, i.e. peak position, FWHM and strength (equivalent width, EW) were measured using the onedspec package within IRAF and are listed in table 5.2. When we plotted the resulting parameters from the continuum-subtracted and the continuum-divided spectra against each other, we

		13micron		
IRAS PSC Name	Source	Center	FWHM	EW
20038-2722	V1943 Sgr	13.1709	0.8251	-0.087
02427-5430	W Hor	13.0921	0.6222	-0.089
14219+2555	RX Boo	13.0343	0.595	-0.11
16387-2700	AX Sco	13.1496	0.7154	-0.102
19194+1734	T Sge	13.0902	1.19	-0.105
20079-0146	V584 Aql	13.0814	0.8272	-0.154
17123+1107	V438 Oph	13.3187	0.9779	-0.099
13022-7650	DL Cha	13.0366	0.5826	-0.114
13303-0656	S Vir	13.1829	0.482	-0.047
13462-2807	W Hya	13.5361	1.383	-0.059
02427-5430	W Hor	13.0729	0.5618	-0.074
14219+2555	RX Boo	13.0063	0.5257	-0.087
16387-2700	AX Sco	13.1792	0.6546	-0.086
17123+1107	V438 Oph	13.3309	0.9305	-0.094
19194+1734	T Sge	13.176	1.246	-0.125
20038-2722	V1943 Sgr	13.1715	0.8011	-0.085
20079-0146	V584 Aql	13.0952	0.8517	-0.159
06551+0322	AZ Mon	13.0425	0.6166	-0.352
10580-1803	R Crt	13.0226	0.5244	-0.234
04361-6210	R Dor	13.0451	0.6018	-0.247
04265+5718	RV Cam	12.9602	0.3701	-0.33
12046-0629	RW Vir	13.0326	0.5232	-0.383
20502+4709	RZ Cyg	13.0028	0.4405	-0.213
22035+3506	SV Peg	12.9902	0.4591	-0.177
00192-2020	T Cet	13.0263	0.58	-0.227
04020-1551	V Eri	12.9965	0.4191	-0.204
02469+5646	W Per	12.9587	0.3339	-0.304

Table 5.2: The 13μm spectral feature parameters for our sample stars.

saw a clear correlation[1] between the two (see figure 5.1). This demonstrates that both continuum-elimination methods are valid and provide equivalent results at least in terms of trends in the spectral features. Stellar parameters were obtained from SIMBAD Astronomical Database and are listed in Appendix A. We then sought correlations between these stellar parameters and 13μm spectral feature parameters.

In addition to the 13μm feature, there are also features in each spectra at 10 and 19μm which may provide clues to the cause of the 13μm feature. The parameters of these features have all been measured using the same technique, and the correlations ere sought amongst these various feature. The resulting determination coefficients were then listed in table 5.4.

5.2 Results and Discussion

Several correlations between the 13μm feature strength and stellar parameters were discovered (not shown). However, under more careful observation, it was observed that W Hya was an outlier that greatly influenced the correlations found. As shown

[1]Following Messenger et al. (2013), we regard a significant correlation as being one for which the determination coefficient (R^2) is greater than a half; i.e. the linear correlation coefficient $R > 0.7$

Stellar Parameter	Peak Position	FWHM	EW
Pulsation Period	0.0009	0.0325	0.0122
Proper motion	0.0444	0.0065	0.0284
Radial velocity	0.1064	0.1634	0.0219
Total velocity	0.0033	0.0108	0.0607
f12	0.0995	0.0605	0.0009
f25	0.0581	0.0338	0.0008
f60	0.0667	0.0411	0.0014
f100	0.0654	0.2983	0.0169
f12/f25	0.2488	0.1744	0.0321
f25/f60	0.0056	0.0020	0.0015
f60/f100	0.0321	0.1554	0.0035
Galactic coordinate longitude	0.0483	0.0383	0.2443
Galactic coordinate latitude	0.0778	0.0006	0.1136
Parallax	0.0108	0.0130	0.0002
B	0.0069	0.0003	0.0042
V	0.0277	0.0047	0.0470
J	0.0453	0.0297	0.0491
H	0.0132	0.0017	0.0133
K	0.0142	0.0025	0.0111

Proper motion is the transverse motion of the star across the sky, whereas radial velocity is the motion in the line of sight measured via Doppler effect; Total velocity is the combination of the two and may effect the interaction with the surrounding medium.
f12, f25, f60 and f100 are the IRAS PSC fluxes (in F_ν)
Galactic coordinates are the location of the star in longitude and latitude where the sun is the center. The primary direction is toward the center of the Milky Way.
B, V, J, H, and K are the magnitudes at the respective filter wavelengths.

Table 5.3: A list of the stellar parameters compared with the 13μm feature parameters, excluding W Hya, and their respective R^2.

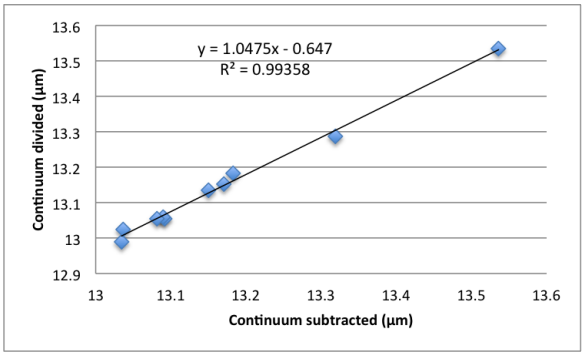

Figure 5.1: Continuum-subtracted vs. continuum-divided spectral feature parameters. The measured 13μm feature peak position for each continuum-elimination technique are plotted against one another. The bestfit linear regression is shown together with the relevant determination coefficient (R^2). The strong correlation between these measured parameters suggests both methods are equivalent to each other.

	13μm Divided			**13μm Subtracted**		
10μm Divided	**Center**	**FWHM**	**EW**	**Center**	**FWHM**	**EW**
Center	0.0006	0.0344	0.0004	0.0000	0.0197	0.0481
FWHM	0.2155	0.0226	0.2823	0.2216	0.1016	0.1964
EW	0.2210	0.0770	0.5218	0.2168	0.1946	0.4423
10μm Subtracted						
Center	0.0019	0.0549	0.1670	0.0040	0.0434	0.0337
FWHM	0.2530	0.0209	0.0036	0.2814	0.0785	0.0025
EW	0.0066	0.2780	0.0149	0.0093	0.3936	0.0057
	19μm Divided			**19μm Subtracted**		
10μm Divided	**Center**	**FWHM**	**EW**	**Center**	**FWHM**	**EW**
Center	0.0030	0.0035	0.0010	0.0523	0.0543	0.1994
FWHM	0.0410	0.1754	0.4220	0.0193	0.2213	0.1461
EW	0.0039	0.1426	0.5272	0.0120	0.1768	0.2281
10μm Subtracted						
Center	0.0077	0.0013	0.1188	0.0078	0.0252	0.0019
FWHM	0.0708	0.0297	0.0065	0.0136	0.0308	0.0593
EW	0.0394	0.1044	0.0904	0.0125	0.1400	0.0514
	19μm Divided			**19μm Subtracted**		
13μm Divided	**Center**	**FWHM**	**EW**	**Center**	**FWHM**	**EW**
Center	0.2332	0.0709	0.0208	0.1523	0.0451	0.0282
FWHM	0.0500	0.0609	0.0058	0.1052	0.0585	0.0001
EW	0.0758	0.0005	0.4359	0.2858	0.0004	0.2692
13μm Subtracted						
Center	0.3068	0.0990	0.0138	0.2051	0.0733	0.0357
FWHM	0.0530	0.0720	0.0004	0.0908	0.1014	0.0002
EW	0.0071	0.0105	0.3203	0.1314	0.0732	0.4102

Table 5.4: A comparison between the 10, 13, and 19μm feature parameters.

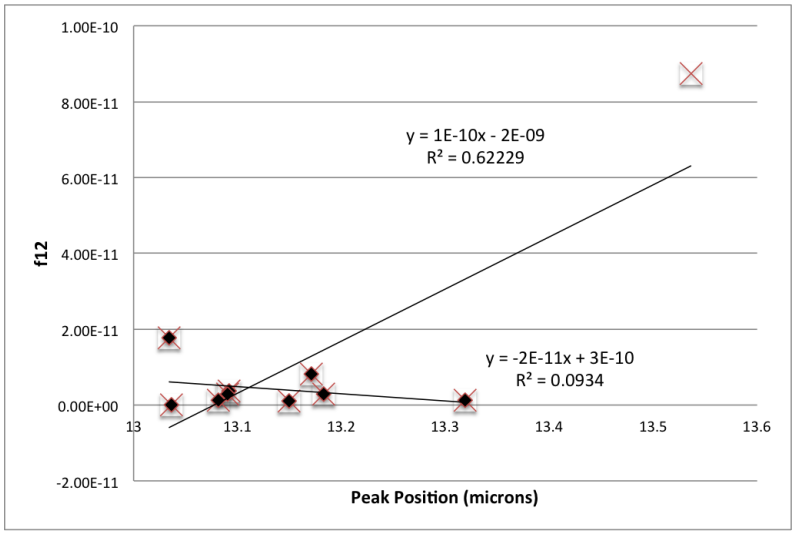

Figure 5.2: Peak position of the 13μm feature plotted against IRAS f12. The data without W Hya is shown as black diamonds while the data with W Hya is shown as red crosses.

in figure 5.2, W Hya is the only reason a correlation was found between the 13μm peak position and IRAS 12μm flux. Including W Hya gives an R^2 value of 0.62229 (a significant correlation), whereas without W Hya, $R^2 = 0.0934$ (no correlation).

The fact that W Hya is an outlier in the sample may be a result of its two separate discrete dust shells suggested in Niyogi et al. (2011) and Wishnow et al. (2010) . One shell is suspected to contain amorphous alumina alone while the other is suspected to contain amorphous alumina and amorphous silicates, where the silicates started to form on the alumina seeds. Therefore, we decided to omit W Hya from our sample for subsequent studies.

Once W Hya was removed, no correlations were found when looking at the stellar parameters vs the 13μm spectral feature parameters. When looking at correlations between the parameters of the various spectral features at 10, 13 and 19μm we see an almost equally disappointing lack of correlations. The only exception is that there is a somewhat significant correlation between the equivalent width of the 13μm feature and that of the 10μm feature. However, this correlation only occurs in the continuum-divided spectra and not in the continuum-subtracted spectra. Therefore there no correlations that are indicative or contraindicative of the carrier of the 13μm. The lack of indicative correlations may be a result of a small sample size, due to our selection criteria. It is also possible that the range of conditions that give

rise to the 13μm feature are such that there are too many variables to get a simple correlation.

Chapter 6

Spatial Variations

Here we investigate whether the strength of the 13μm feature has any spatial variations relative to the location from the star for O-rich AGB stars.

6.1 Spatially-resolved Spectra

The sample we use was first presented in Niyogi et al. (2011), which investigated the spatial distribution of changes in the broad 9–12μm feature in 7 O-rich AGB stars. The two least complicated spectra from that observation set were chosen for our sample. Spectra of our sample were obtained using the MICHELLE on Gemini North. We used long-slit spectroscopy to obtain spatially-resolved spectra for several stars. The data was reduced in the standard manner using the Gemini IRAF package. For imaging, the raw frames were stacked and the images were calibrated using the observation of the photometric standard star to convert from ADU to Jansky or to Jansky per square arc-second, as appropriate. The expected fluxes of the standard star were taken from Cohen et al. (1999). For spectroscopy the telluric correction and absolute calibration were carried out by taking the ratio of the object spectrum to the standard star spectrum, with a small wavelength shift and scaling for air-mass as required to remove the atmospheric bands. We then multiplied through by the expected spectrum of the standard star, again taken from the spectrophotometric templates of Cohen et al. (1999).

Next, the 2-d spectrum was sliced (that is, the 2-d data was reduced to a series

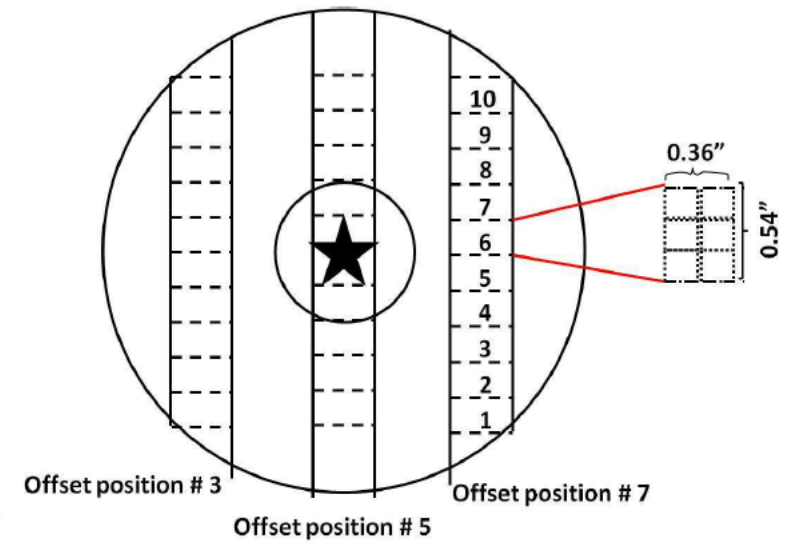

Figure 6.1: Cartoon schematic of the slices produced for spacial resolution [Niyogi et al., 2011].

of 1-d spectra corresponding to positions in the shell). Ten of these slices were produced, each 0.4 arcseconds in width. The process was repeated 10 times across the star until a 10 by 10 grid of spectra was obtained for each star, as shown in figure 6.1.

As in described in chapter 3, it is necessary to isolate the spectral features by eliminating the continuum contribution to the spectrum. Consequently we followed the same method described in chapter 5 to fit a power-law continuum, which was then subtracted. Using the onedspec package within IRAF, we measured the 13μm spectral feature parameters. The 13μm spectral feature parameters were then plotted on a grid based on the location of the spectra the feature belonged to as shown in figure 6.2. In this way we can to determine whether the 13μm feature has any correlation with the distance the dust is from the star. A correlation with the distance from the star would be indicative of the dust formation environment around the star and thus the carrier of the feature.

6.2 Results

Figures 6.3 and 6.4 show graphically how the peak position, equivalent width and FWHM vary spatially in our two sources. The spatial resolution for R Hya (fig-

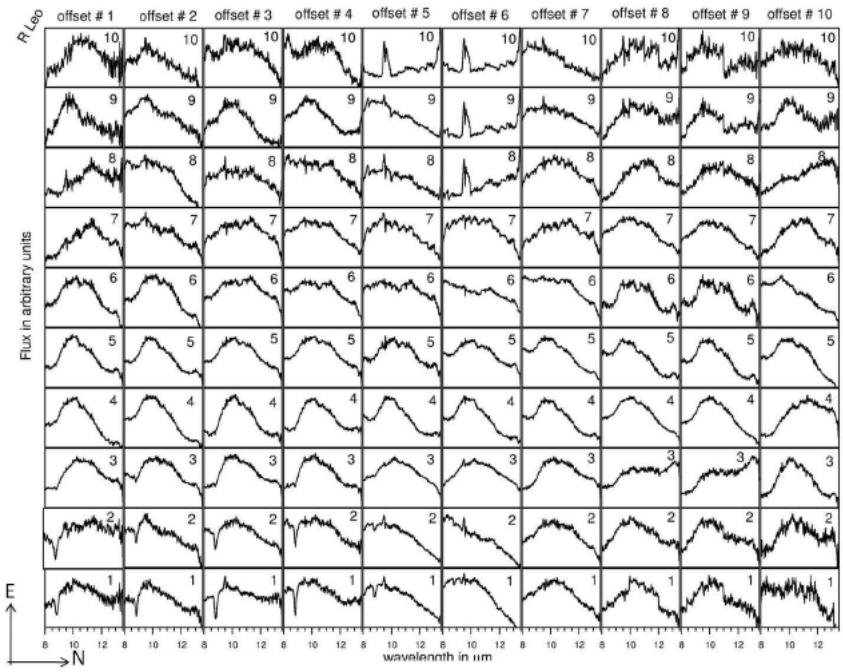

Figure 6.2: The spatially resolved IR spectra of R Leo shown position by position [Niyogi et al., 2011].

ure 6.3) shows the peak position of the 13μm feature appearing to shift to shorter wavelengths as we move away from the star, with the shift varying from 13.53 to 12.46μm. Meanwhile, for R Hya the equivalent width (or strength) of the 13μm feature was found to be lower toward the star and larger further away from the star. This implies the 13μm feature is stronger further out from the star. On the other hand, the FWHM is more evenly distributed across the space around the star with just a hint that the width is narrower in the central columns of the grid.

For R Leo, the peak position of the 13μm (figure 6.4) is much more uniform; no general trend is observed. In contrast, there is a clear trend for the equivalent width such that it decreases closer to the star. This is very similar to that seen for R Hya. Meanwhile, the full width half maximum (FWHM) of R Leo gets smaller as we move towards the central star. This would mean that the feature is becoming sharper as we move towards the center star, which was not seen for R Hya.

Peak Position

	28	29	30	31	32	33	34	35	36	37	38
1	13.5325	13.0155	12.6015		12.8984	12.7245	12.7481	12.4947	12.7843	12.5148	12.9539
2	12.9424	12.9565	12.7643	12.9114	12.9417	12.6403	12.5349	13.1004		12.7857	
3	12.5537	13.0521	13.2271	12.9507	12.8702	12.5469	12.8626	13.2174		12.8947	12.9626
4	12.9596	12.8884	12.9183	12.9766	12.9811	12.8455	13.0238	12.9935	12.7052	13.0426	12.9875
5	12.8883	12.9966	12.9408	12.9156	13.0313	12.9887	12.999	12.9811	12.9973	13.0195	13.0051
6	12.977	13.0053	13.0252	12.986	12.9472	13.0049	12.9297	12.9198	12.9571	12.9605	12.9555
7	12.9442	12.9787	12.9462	13.0027	12.9175	12.8598	12.9524	12.9119	12.9218	12.9152	12.9588
8	12.886	13.0351	12.9294	12.9507		12.755	12.9386	12.9114	12.9147	12.8624	12.9415
9	12.7218	13.0427	13.0848	12.9252	12.8892	12.5593	12.7428	12.8875	12.848	12.9422	12.9771
10	12.744		13.0189		12.4638	12.5695	12.535			12.7451	12.7881

EW

	28	29	30	31	32	33	34	35	36	37	38
1	-0.462		-1.012		-0.064	-0.047	-0.005	-0.555	-0.239	-1.068	-0.477
2	-0.108	-0.228	-0.094	-0.067	-0.052	-0.061	-0.009	-1.017		-0.379	
3		-0.137	-0.359	-0.124	-0.231	-0.01	-0.03	-0.177		-0.194	-0.26
4	-0.047	-0.061	-0.049	-0.08	-0.049	-0.026	-0.051	-0.126	-0.033	-0.056	-0.098
5	-0.032	-0.075	-0.059	-0.055	-0.039	-0.036	-0.04	-0.034	-0.072	-0.043	-0.056
6	-0.036	-0.071	-0.061	-0.048	-0.051	-0.037	-0.03	-0.05	-0.065	-0.059	-0.06
7	-0.021	-0.054	-0.048	-0.039	-0.099	-0.1	-0.037	-0.075	-0.074	-0.044	-0.039
8	-0.046	-0.08	-0.078	-0.043		-0.048	-0.038	-0.056	-0.024	-0.21	-0.077
9	-0.071	-0.279	-0.092	-0.038	-0.013	-0.01	-0.039	-0.114	-0.064	-0.106	-0.123
10	-0.286		-0.309		-0.099	-0.02	-0.006			-0.167	-0.105

FWHM

	28	29	30	31	32	33	34	35	36	37	38
1	3.272	0.4872	3.245		0.4152	0.5509	0.0273	1.515	1.005	1.319	0.8783
2	1.006	0.8628	0.7079	0.3665	0.361	0.6476	0.0498	0.9172		1.901	
3		0.5303	0.9043	1.224	1.003	0.1374	0.7101	0.8073		0.8076	0.9982
4	1.046	0.5884	0.7387	0.8808	0.7839	0.8631	0.6799	0.938	1.628	0.4211	0.7683
5	0.7355	0.8214	0.6774	0.7202	0.5464	0.6912	0.6101	0.5163	0.7033	0.4617	0.5005
6	0.4461	0.6202	0.5209	0.4798	0.5738	0.4443	0.6139	0.6557	0.6549	0.5755	0.6277
7	0.3776	0.4947	0.5721	0.4832	0.8118	0.8334	0.3567	0.7059	0.6856	0.4482	0.4539
8	0.5134	0.4726	0.5602	0.4235		0.7792	0.4171	0.5236	0.3182	1.125	0.6932
9	0.7929	0.7985	0.7612	0.4294	0.2749	0.1008	0.6602	0.8527	0.5701	0.6707	1.067
10	2.66		1.263		1.232	0.138	0.0492			1.147	0.8738

Figure 6.3: Peak position, equivalent width (EW), full width half maximum (FWHM) findings for the spatial resolution R Hya.

Peak Position

	0	1	2	3	4	5	6	7	8	9	10
1	13.1811	13.0021	13.1296	12.9657			12.9116	13.0444	12.9864	13.505	12.953
2	13.0878	13.0672	13.1178				12.9767	13.0459	12.9657	12.9626	12.9902
3	13.1256	13.1095	13.0595	13.0974	12.9656	13.0727	12.9936	12.9943	13.029	13.1501	13.0337
4	13.0977	13.0989	13.0872	13.1824	13.109	13.0928	13.0961	13.0986	13.0461	13.035	13.0368
5	13.0707	13.0032	13.112	12.9975	13.03	13.0674	13.0697	13.0671	13.081	13.0573	13.0297
6	13.0575	13.069	13.0227	12.981	12.9875	13.0143	12.9987	13.0717	13.0263	13.0148	12.9956
7	13.0399	13.0084	12.9877	12.9814	12.9566	12.944	12.9466	12.9522	12.9235	12.9872	12.9818
8	13.0424	13.0868	12.9656	12.9348		12.802	12.9495	12.8259	12.9893	12.981	12.8086
9	13.0379	13.1017	13.1216			12.6389	12.9507		12.9606	13.02	13.0789
10		13.0068	13.0864	13.2153				13.0083		13.1226	12.9439

EW

	0	1	2	3	4	5	6	7	8	9	10
1	-0.222	-0.238	-0.279	-0.104			-0.03	-0.099	-0.053	-0.046	-0.097
2	-0.047	-0.067	-0.051				-0.015	-0.044	-0.025	-0.06	-0.032
3	-0.045	-0.041	-0.025	-0.024	-0.024	-0.028	-0.011	-0.037	-0.048	-0.045	-0.039
4	-0.033	-0.033	-0.038	-0.046	-0.025	-0.027	-0.021	-0.022	-0.024	-0.028	-0.021
5	-0.031	-0.036	-0.039	-0.024	-0.027	-0.019	-0.027	-0.029	-0.029	-0.022	-0.023
6	-0.024	-0.033	-0.012	-0.012	-0.015	-0.017	-0.011	-0.038	-0.032	-0.04	-0.023
7	-0.043	-0.036	-0.018	-0.023	-0.015	-0.027	-0.02	-0.03	-0.025	-0.055	-0.036
8	-0.079	-0.042	-0.017	-0.015		-0.042	-0.014	-0.026	-0.014	-0.038	-0.118
9	-0.077	-0.462	-0.063			-0.034	-0.011		-0.031	-0.081	-0.139
10		-0.169	-0.041	-0.077				-0.052		-0.122	-0.046

FWHM

	0	1	2	3	4	5	6	7	8	9	10
1	0.5573	0.6155	0.7784	0.9989			0.2985	0.4862	0.3966	0.2435	0.5076
2	0.361	0.3551	0.3841				0.3143	0.4455	0.2968	0.5468	0.4757
3	0.3834	0.381	0.4178	0.3817	0.5767	0.4965	0.3217	0.5614	0.5345	0.4029	0.4321
4	0.3904	0.3588	0.5874	0.6201	0.3968	0.4454	0.3391	0.36	0.5838	0.3933	0.3905
5	0.3882	0.4989	0.3812	0.5146	0.4751	0.3034	0.3521	0.4433	0.3615	0.3774	0.4579
6	0.35	0.3998	0.3101	0.2868	0.4129	0.3183	0.2973	0.4697	0.4471	0.5517	0.4406
7	0.5147	0.4165	0.3376	0.4493	0.2309	0.2724	0.2626	0.4594	0.3531	0.5359	0.4774
8	0.5449	0.3966	0.3454	0.3159		0.6432	0.2663	0.6131	0.2911	0.4612	1.013
9	0.3968	0.7388	0.4613			0.4206	0.2623		0.3753	0.503	1.168
10		0.4686	0.5053	0.8173				0.4104		0.346	0.2574

Figure 6.4: Peak position, equivalent width (EW), full width half maximum (FWHM) findings for the spatial resolution R Leo

6.3 Discussion

In both objects studied here the 13μm feature is weakest (has the most positive equivalent width) closest to the central star. This observation suggests that whatever the mineral is that gives rise to the 13μm feature forms best furthest away from the star. Under the classic condensation sequence corundum (Al_2O_3) is formed closer to the star than silicates and then forms the seed on which silicates can form. Under such a scenario, we would expect the 13μm feature to be strongest close to the star if it is due to corundum. However, this is the opposite of what we see, suggesting that corundum is not a good candidate for the carrier of this feature. Silica would be expected to form further away from the central star where the temperatures and densities are lower, which is consistent with the increasing 13μm feature strength with distance from the central star.

For R Leo the peak position is not very diagnostic, whereas for R Hya the peak position is shorter closer to the central column. Moreover, for R Leo the FWHM suggests a broadening of the feature as we move further out from the star, but the FWHM data for R Hya is also not very diagnostic.

Speck (1998) presented laboratory spectra that demonstrate that the crystallinity and precise crystal structure can change the position and width of the 13μm, with crystalline samples having the narrowest features. Therefore the variation in the FWHM may be due to changes in the type of silica that forms or whether it can be annealed.

It is interesting to note that Niyogi et al. (2011) found that the 10μm feature of R Hya moves toward lower wavelengths and has a smaller FWHM (is narrower) closer towards the star. The trend is similar to the one we have observed for the 13μm feature's EW for R Hya. Perhaps the same mechanism that is causing the 13μm feature's strength to increase further from the star is causing the 10μm feature (attributed to the Si-O bond stretching) to become less narrow and move toward larger wavelengths.

Silica may originate during rapid cooling under non-equilibrium conditions (see section 4.4) which is the condition we would have further out from the star. Whereas the higher densities closer to the star could give rise to equilibrium products such

as simpale magensiums silicate glasses. A more chaotic condensation process would produce many different minerals including silica, different silicates and oxides that would produce both the stronger 13μm and the broader 9–12μm feature. Therefore the data presented here supports silica rather tha corundum as the carrier of the 13μm feature.

Bibliography

[Alexander and Ferguson, 1994] Alexander, D. and Ferguson, J. (1994). Low-temperature rosseland opacities. *The Astrophysical Journal*, 437:879–891. 2.3.2

[Begemann et al., 1997] Begemann, B., Dorschner, J., Henning, T., Mutschke, H., Guertler, J., Koempe, C., and Nass, R. (1997). Aluminum oxide and the opacity of oxygen-rich circumstellar dust in the 12-17 micron range. *The Astrophysical Journal*, 476(1):199. 4.2

[Bussmann et al., 2009] Bussmann, R., Dey, A., Borys, C., Desai, V., Jannuzi, B., Le Floc'h, E., Melbourne, J., Sheth, K., and Soifer, B. (2009). Infrared luminosities and dust properties of z 2 dust-obscured galaxies. *The Astrophysical Journal*, 705(1):184. 1

[Cain, 2009] Cain, F. (2009). Universe today. (document), 2.2

[Carroll and Ostlie, 2007] Carroll, B. W. and Ostlie, D. A. (2007). *An Introduction to Modern Astrophysics*. Pearson Addison Wesley, second edition. 2.3.2, 3.1

[Cline, 2010] Cline, T. (2010). Spectroscopy. (document), 3.2

[Cohen et al., 1999] Cohen, M., Walker, R. G., Carter, B., Hammersley, P., Kidger, M., and Noguchi, K. (1999). Spectral irradiance calibration in the infrared. x. a self-consistent radiometric all-sky network of absolutely calibrated stellar spectra. *The Astronomical Journal*, 117(4):1864. 6.1

[DePew et al., 2006] DePew, K., Speck, A., and Dijkstra, C. (2006). Astromineralogy of the 13 μm feature in the spectra of oxygen-rich asymptotic giant branch

stars. i. corundum and spinel. *The Astrophysical Journal*, 640(2):971. 4.2, 4.3, 4.4

[Draine, 2003] Draine, B. (2003). Scattering by interstellar dust grains. i. optical and ultraviolet. *The Astrophysical Journal*, 598(2):1017. 1

[Fabian et al., 2001] Fabian, D., Henning, T., Jäger, C., Mutschke, H., Dorschner, J., and Wehrhan, O. (2001). Steps toward interstellar silicate mineralogy. *Astronomy and Astrophysics*, 378(1):228–238. 4.4

[Feast and Whitelock, 1987] Feast, M. and Whitelock, P. (1987). Mira variables and the galactic bulge population. In *Late Stages of Stellar Evolution*, pages 33–46. Springer. 4.1.1

[Gail and Sedlmayr, 1999] Gail, H.-P. and Sedlmayr, E. (1999). Mineral formation in stellar winds. i. condensation sequence of silicate and iron grains in stationary oxygen rich outflows. *Astronomy and Astrophysics*, 347:594–616. 2.3.3, 4.4

[Glaccum, 1995] Glaccum, W. (1995). Infrared dust features of late-type stars and planetary nebulae. In *From Gas to Stars to Dust*, volume 73, pages 395–396. 4.2

[Habing, 1996] Habing, H. (1996). Circumstellar envelopes and asymptotic giant branch stars. *The Astronomy and Astrophysics Review*, 7(2):97–207. 4.1.1

[Habing and Olofsson, 2004] Habing, H. J. and Olofsson, H., editors (2004). *Asymptotic Giant Branch Stars*. Springer. 2.3

[Hackwell, 1972] Hackwell, J. (1972). Long wavelength spectrometry and photometry of m, s and c-stars. *Astronomy and Astrophysics*, 21:239–248. 4.2

[Heras and Hony, 2005] Heras, A. and Hony, S. (2005). Oxygen-rich agb stars with optically thin dust envelopes. *Astronomy and Astrophysics*, 439(1):171–182. 4.3

[Höfner and Dorfi, 1997] Höfner, S. and Dorfi, E. (1997). Dust formation in winds of long-period variables. iv. atmospheric dynamics and mass loss. *Astronomy and Astrophysics*, 319:648–654. 2.3.2

[Hron et al., 1997] Hron, J., Aringer, B., and Kerschbaum, F. (1997). Semiregular variables of types sra and srb. silicate dust emission features. *Astronomy and Astrophysics*, 322:280–290. 4.1.1

[Justtanont et al., 1998] Justtanont, K., Feuchtgruber, H., De Jong, T., Cami, J., Waters, L., Yamamura, I., and Onaka, T. (1998). Discovery of co_2 emission in agb stars with the 13mu m dust feature. *Astronomy and Astrophysics*, 330:L17–L20. 4.1.1

[Kerschbaum and Hron, 1992] Kerschbaum, F. and Hron, J. (1992). Semiregular variables of types sra and srb-basic properties in the visual and the iras-range. *Astronomy and Astrophysics*, 263:97–112. 4.1.1

[Kozasa and Sogawa, 1997] Kozasa, T. and Sogawa, H. (1997). Formation of dust grains in circumstellar envelopes of oxygen-rich agb stars. *Astrophysics and Space Science*, 251(1-2):165–170. 4.2

[Kozasa and Sogawa, 1998] Kozasa, T. and Sogawa, H. (1998). Formation of al2o3 grains and the 13μm feature in circumstellar envelopes of oxygen-rich agb stars. In *Astrophysics and space science*, pages 437–443. Springer. 4.2

[Krügel, 2008] Krügel, E. (2008). *An introduction to the physics of interstellar dust*. Taylor & Francis. 1

[Kwok, 2004] Kwok, S. (2004). The synthesis of organic and inorganic compounds in evolved stars. *Nature*, 430(7003):985–991. 2.2

[Little-Marenin and Little, 1988] Little-Marenin, I. R. and Little, S. J. (1988). Emission features in iras low-resolution spectra of ms, s and sc stars. *The Astrophysical Journal*, 333:305–315. 3.3

[Little-Marenin and Little, 1990] Little-Marenin, I. R. and Little, S. J. (1990). Emission features in iras lrs spectra of m mira variables. *The Astronomical Journal*, 99:1173–1186. 4.2

[Lodders and Fegley Jr, 1999] Lodders, K. and Fegley Jr, B. (1999). Condensation chemistry of circumstellar grains. In *Asymptotic giant branch stars*, volume 191, page 279. 2.3.3, 4.4

[Maldoni et al., 2005] Maldoni, M., Ireland, T., Smith, R., and Robinson, G. (2005). Al2o3 dust in oh/ir stars. *Monthly Notices of the Royal Astronomical Society*, 362(3):872–878. 4.2

[Mattei et al., 1997] Mattei, J. A., Foster, G., Hurwitz, L. A., Malatesta, K. H., Willson, L. A., and Mennessier, M.-O. (1997). Classification of red variables. In *Hipparcos-Venice'97*, volume 402, pages 269–274. 4.1.1

[Moore, 1978] Moore, Collins, D. (1978). Characteristic wavelengths of infrared absorption for some chemical bonds. (document), 3.1

[Nagahara and Ozawa, 2009] Nagahara, H. and Ozawa, K. (2009). Condensation kinetics of forsterite and metal and chemical fractionation in the proto solar nebula. In *Lunar and Planetary Institute Science Conference Abstracts*, volume 40, page 2158. 4.4

[Niyogi et al., 2011] Niyogi, S. G., Speck, A. K., and Onaka, T. (2011). A temporal study of the oxygen-rich pulsating variable asymptotic giant branch star, t cep: Investigation on dust formation and dust properties. *The Astrophysical Journal*, 733(2):93. (document), 3.2.1, 5.2, 6.1, 6.1, 6.2, 6.3

[Onaka et al., 1989] Onaka, T., De Jong, T., and Willems, F. (1989). A study of m mira variables based on iras lrs observations. i-dust formation in the circumstellar shell. *Astronomy and Astrophysics*, 218:169–179. 4.2

[Rietmeijer et al., 1999] Rietmeijer, F. J., Nuth III, J. A., and Karner, J. M. (1999). Metastable eutectic condensation in a mg-fe-sio-h2-o2 vapor: analogs to circumstellar dust. *The Astrophysical Journal*, 527(1):395. 4.4

[Salpeter, 1974] Salpeter, E. (1974). Nucleation and growth of dust grains. *The Astrophysical Journal*, 193:579–584. 4.2

[Sedlmayr, 1989] Sedlmayr, E. (1989). Dust condensation in stellar outflows. In *Interstellar Dust*, pages 467–478. Springer. 4.2

[Sloan et al., 2003] Sloan, G., Kraemer, K. E., Goebel, J., and Price, S. D. (2003). Guilt by association: the 13 micron dust emission feature and its correlation to other gas and dust features. *The Astrophysical Journal*, 594(1):483. 4.3

[Sloan et al., 1996] Sloan, G., LeVan, P., and Little-Marenin, I. (1996). Sources of the 13 micron feature associated with oxygen-rich circumstellar dust. *The Astrophysical Journal*, 463:310. 4.1

[Sloan et al., 2009] Sloan, G., Matsuura, M., Zijlstra, A., Lagadec, E., Groenewegen, M., Wood, P., Szyszka, C., Bernard-Salas, J., and van Loon, J. T. (2009). Dust formation in a galaxy with primitive abundances. *Science*, 323(5912):353–355. 1

[Sloan and Price, 1995] Sloan, G. and Price, S. (1995). Silicate emission at 10 microns in variables on the asymptotic giant branch. *The Astrophysical Journal*, 451:758. 3.3, 5.1

[Speck, 1998] Speck, A. (1998). The mineralogy of dust around evolved stars. 6.3

[Speck, 2012] Speck, A. (2012). Variable stars and the asymptotic giant branch: Stellar pulsations, dust production, and mass loss. *Journal of the American Association of Variable Star Observers (JAAVSO)*, 40:244. 2.3.2

[Speck et al., 2000] Speck, A., Barlow, M., Sylvester, R., and Hofmeister, A. (2000). Dust features in the 10-m infrared spectra of oxygen-rich evolved stars. *Astronomy and Astrophysics Supplement Series*, 146(3):437–464. 3.3, 4.4

[Speck et al., 2006] Speck, A. K., Cami, J., Markwick-Kemper, C., Leisenring, J., Szczerba, R., Dijkstra, C., Van Dyk, S., and Meixner, M. (2006). The unusual spitzer spectrum of the carbon star iras 04496–6958: A different condensation sequence in the lmc? *The Astrophysical Journal*, 650(2):892. 3.2

[Speck et al., 2009] Speck, A. K., Corman, A. B., Wakeman, K., Wheeler, C. H., and Thompson, G. (2009). Silicon carbide absorption features: dust formation

in the outflows of extreme carbon stars. *The Astrophysical Journal*, 691(2):1202. 2.3.2

[Speck et al., 2008] Speck, A. K., Whittington, A. G., and Tartar, J. B. (2008). The cosmic crystallinity conundrum: Clues from iras 17495–2534. *The Astrophysical Journal Letters*, 687(2):L91. 2.3.2

[Stencel et al., 1990] Stencel, R. E., Nuth III, J. A., Little-Marenin, I. R., and Little, S. J. (1990). The formation and annealing of circumstellar dust, as gauged by iras low-resolution spectra and the microwave maser chronology. *The Astrophysical Journal*, 350:L45–L48. 2.3.3

[Swamy, 2005] Swamy, K. K. (2005). *Dust in the Universe: Similarities and Differences*, volume 7. World Scientific Publishing Company. 1

[Thompson et al., 2006] Thompson, G. D., Corman, A. B., Speck, A. K., and Dijkstra, C. (2006). Challenging the carbon star dust condensation sequence: Anarchist c stars. *The Astrophysical Journal*, 652(2):1654. 3.2

[Tielens, 1990] Tielens, A. (1990). Towards a circumstellar silicate mineralogy. *From Miras to Planetary Nebulae*, pages 186–200. (document), 2.3.3, 2.6, 4.2

[Vardya et al., 1986] Vardya, M., De Jong, T., and Willems, F. (1986). Iras low-resolution spectrograph observations of silicate and molecular sio emission in mira variables. *The Astrophysical Journal*, 304:L29–L32. 4.2

[Videen and Kocifaj, 2002] Videen, G. and Kocifaj, M. (2002). *Optics of cosmic dust*, volume 79. Kluwer Academic Pub. 1

[Wishnow et al., 2010] Wishnow, E., Townes, C., Walp, B., and Lockwood, S. (2010). The dust surrounding w hydrae. *The Astrophysical Journal Letters*, 712(2):L135. 5.2

[Woitke, 2006a] Woitke, P. (2006a). The chaotic winds of cool giants. (document), 2.4

[Woitke, 2006b] Woitke, P. (2006b). Too little radiation pressure on dust in the winds of oxygen-rich agb stars. *Astronomy and Astrophysics*, 460(2):L9–L12. 1

Appendix A

Stellar Parameters from SIMBAD.

This is a table of the stellar parameters for the sample stars chosen for the variations in the 13μm feature test.

IRAS PSC Name	Source	TDT		Variable Type		Spectral Type	SE Class	Period (days)
20038-2722	V1943 Sgr	85700514	-	Lb	Pulsating Variable	M7 III	3	-
02427-5430	W Hor	17902728	75600502	SRb	Semi-Regular Pulsating	M...C	3	137
14219+2555	RX Boo	8201905	-	SRb	Semi-Regular Pulsating	M7.5	3	340
16387-2700	AX Sco	12101602	-	SRb	Semi-Regular Pulsating	M5III	3	138
19194+1734	T Sge	12000604	73201510	SRb	Semi-Regular Pulsating	M4-6.5	3	166
20079-0146	V584 Aql	54200304	73200811	Lb	Pulsating Variable	M8	3	-
17123+1107	V438 Oph	11601203	81001108	SRb	Semi-Regular Pulsating	M8 D	3	170
13022-7650	DL Cha	62804032	-	SRb	Semi-Regular Pulsating	M6 III	3	-
13303-0656	S Vir	25302224	-	M	Mira Cet	M6-9.5 IIIe	3	375
13462-2807	W Hya	8902004	41800303	SRa	Semi-Regular Pulsating	M7.5-9ep	3	361
02427-5430	W Hor	17902728	75600502	SRb	Semi-Regular Pulsating	M...C	3	137
14219+2555	RX Boo	8201905	-	SRb	Semi-Regular Pulsating	M7.5	3	340
16387-2700	AX Sco	12101602	-	SRb	Semi-Regular Pulsating	M5III	3	138
17123+1107	V438 Oph	11601203	81001108	SRb	Semi-Regular Pulsating	M8 D	3	170
19194+1734	T Sge	12000604	73201510	SRb	Semi-Regular Pulsating	M4-6.5	3	166
20038-2722	V1943 Sgr	85700514	-	Lb	Pulsating Variable	M8	3	-
20079-0146	V584 Aql	54200304	73200811	Lb	Pulsating Variable	M8	3	-
06551+0322	AZ Mon	-	-		Mira Cet	M9 D	3	-
10580-1803	R Crt	-	-	SRb	Semi-Regular Pulsating	M7 III	3	-
04361-6210	R Dor	-	-	SRb	Semi-Regular Pulsating	M8 IIIe	7	338
04265+5718	RV Cam	-	-	SRb	Semi-Regular Pulsating	M4 II-III	6	101
12046-0629	RW Vir	-	-	SRb	Pulsating Variable	M5 IIIc	3	-
20502+4709	RZ Cyg	-	-	Sra	Semi-Regular Pulsating	M7 D	3	-
22035+3506	SV Peg	17301206	74500605	SRb	Semi-Regular Pulsating	M7	3	-
00192-2020	T Cet	-	-	SRc	Semi-Regular Pulsating	M5-6SIIe	1	159
04020-1551	V Eri	-	-		Semi-Regular Pulsating	M5/M6IV C	3	-
02469+5646	W Per	-	-	SRc	Semi-Regular Pulsating	M4.5Iab	5	485

IRAS PSC Name	Source	Proper Motion			Radial Velocity (km/s)	Pythagorean	IRAS	
							f12	f25
20038-2722	V1943 Sgr	24.87	-44.82	0.71 0.48 0	-	-	394.70	152.40
02427-5430	W Hor	-10.80	-3.40	3.20 3.00 0	-	-	181.00	99.85
14219+2555	RX Boo	21.21	-48.79	0.50 0.46 0	-9.42	23.21	846.50	419.30
16387-2700	AX Sco	-7.94	-5.47	1.13 0.87 0	-45.00	45.70	47.22	20.01
19194+1734	T Sge	2.66	-28.01	0.71 0.69 0	4.00	4.80	140.20	65.67
20079-0146	V584 Aql	-3.10	-12.10	1.80 1.80 177			60.22	28.86
17123+1107	V438 Oph	4.55	7.04	1.03 0.79 0	-7.00	8.35	61.56	26.69
13022-7650	DL Cha	-	-	-	-	-	1.95	0.71
13303-0656	S Vir	-17.84	2.67	0.73 0.46 0	10.00	20.45	135.00	54.82
13462-2807	W Hya	-49.31	-59.71	1.48 1.04 0	42.30	64.97	4200.00	1189.00
02427-5430	W Hor	-10.80	-3.40	3.20 3.00 0			181.00	99.85
14219+2555	RX Boo	21.21	-48.79	0.50 0.46 0	-9.42	23.21	846.50	419.30
16387-2700	AX Sco	-7.94	-5.47	1.13 0.87 0	-45.00	45.70	47.22	20.01
17123+1107	V438 Oph	4.55	7.04	1.03 0.79 0	-7.00	8.35	61.56	26.69
19194+1734	T Sge	2.66	-28.01	0.71 0.69 0	4.00	4.80	140.20	65.67
20038-2722	V1943 Sgr	24.87	-44.82	0.71 0.48 0	-	-	394.70	152.40
20079-0146	V584 Aql	-6.10	-12.80	1.0 1.0 4	-	-	60.22	28.86
06551+0322	AZ Mon	-	-	-	-	-	36.63	15.67
10580-1803	R Crt	-28.79	-2.06	0.83 0.74 0	18.00	33.95	637.90	307.70
04361-6210	R Dor	-68.46	-71.22	0.78 0.73 8	26.10	73.27	5157.00	1594.00
04265+5718	RV Cam	-5.67	4.27	0.68 0.68 76	-21.00	21.75	58.68	34.58
12046-0629	RW Vir	-28.46	16.41	0.40 0.29 0	-	-	86.50	36.12
20502+4709	RZ Cyg	-	-	-	-47.00	-	104.90	62.22
22035+3506	SV Peg	12.27	-9.73	1.17 1.24 0	-1.00	12.31	264.70	146.20
00192-2020	T Cet	61.91	-12.81	1.01 0.50 86	29.10	68.41	197.80	55.75
04020-1551	V Eri	-3.80	-16.39	0.97 0.95 0	-3.00	4.84	326.40	183.60
02469+5646	W Per	-1.23	-5.23	1.05 0.99 24	-50.20	50.22	90.58	78.86

IRAS PSC Name	Source	IRAS						ICRS Coord.	
		f60	f100	f12/f25	f25/f60	f60/f100			
20038-2722	V1943 Sgr	28.41	13.65	2.59	5.36	2.08	Optical	20 06 55.24418 -27 13 29.7616	6.23 4.22 0
02427-5430	W Hor	11.01	4.22	1.81	9.07	2.61	~	02 44 14.7520 -54 18 04.108	29.81 28.12 0
14219+2555	RX Boo	69.19	25.80	2.02	6.06	2.68	~	14 24 11.6270 +25 42 13.401	7.90 4.06 134
16387-2700	AX Sco	3.15	13.94	2.36	6.35	0.23	Optical	16 41 49.75675 -27 06 19.3379	1.16 0.68 0
19194+1734	T Sge	11.80	73.42	2.13	5.57	0.16	Optical	19 21 42.04821 +17 39 59.8077	6.24 6.06 0
20079-0146	V584 Aql	4.84	2.05	2.09	5.96	2.36	~	20 10 29.8277 -01 37 40.853	22.93 21.24 90
17123+1107	V438 Oph	4.45	3.72	2.31	6.00	1.20	Optical	17 14 39.77832 +11 04 09.8939	0.85 0.71 0
13022-7650	DL Cha	4.85	2.41	2.75	0.15	2.01	Infrared	13 00 04.68 -78 28 57.7	280 90 0
13303-0656	S Vir	8.25	2.30	2.46	6.64	3.59	~	13 33 00.1081 -07 11 41.017	14.32 8.18 103
13462-2807	W Hya	195.00	72.25	3.53	6.10	2.70	~	13 49 01.9980 -28 22 03.488	10.50 6.67 110
02427-5430	W Hor	11.01	4.22	1.81	9.07	2.61	~	02 44 14.7520 -54 18 04.108	29.81 28.12 0
14219+2555	RX Boo	69.19	25.80	2.02	6.06	2.68	~	14 24 11.6270 +25 42 13.401	7.90 4.06 134
16387-2700	AX Sco	3.15	13.94	2.36	6.35	0.23	Optical	16 41 49.75675 -27 06 19.3379	1.16 0.68 0
17123+1107	V438 Oph	4.45	3.72	2.31	6.00	1.20	Optical	17 14 39.77832 +11 04 09.8939	0.85 0.71 0
19194+1734	T Sge	11.80	73.42	2.13	5.57	0.16	Optical	19 21 42.04821 +17 39 59.8077	6.24 6.06 0
20038-2722	V1943 Sgr	28.41	13.65	2.59	5.36	2.08	Optical	20 06 55.24418 -27 13 29.7616	6.23 4.22 0
20079-0146	V584 Aql	4.84	2.05	2.09	5.96	2.36	~	20 10 29.8277 -01 37 40.853	22.93 21.24 90
06551+0322	AZ Mon	2.48	8.14	2.34	6.32	0.30	Infrared	06 57 45.19 +03 18 09.3	290 290 89
10580-1803	R Crt	49.73	19.73	2.07	6.19	2.52	Optical	11 00 33.85289 -18 19 29.5802	7.31 6.50 53
04361-6210	R Dor	243.50	83.45	3.24	6.55	2.92	~	04 36 45.5923 -62 04 37.756	6.77 6.09 4
04265+5718	RV Cam	7.71	3.95	1.70	4.49	1.95	~	04 30 41.6787 +57 24 42.263	6.25 6.09 148
12046-0629	RW Vir	4.68	1.80	2.39	7.72	2.60	Optical	12 07 14.90311 -06 45 56.0663	3.52 2.55 0
20502+4709	RZ Cyg	11.31	36.59	1.69	5.50	0.31	Infrared	20 51 53.18 +47 21 20.4	290 290 0
22035+3506	SV Peg	23.61	9.94	1.81	6.19	2.38	Optical	22 05 42.08385 +35 20 54.5280	10.89 10.27 90
00192-2020	T Cet	14.41	4.76	3.55	3.87	3.03	~	00 21 46.2737 -20 03 28.885	8.76 4.23 87
04020-1551	V Eri	23.63	7.16	1.78	7.77	3.30	Optical	04 04 18.79987 -15 43 30.5145	8.51 8.33 60
02469+5646	W Per	14.87	5.01	1.15	5.30	2.97	~	02 50 37.8911 +56 59 00.251	9.17 8.92 29

IRAS PSC Name	Source	FK5 Coord.		FK4 Coord.	
20038-2722	V1943 Sgr	20 06 55.244 -27 13 29.76	6.23 4.22 0	20 03 51.92 -27 22 09.0	36.04 24.37 0
02427-5430	W Hor	02 44 14.752 -54 18 04.11	29.81 28.12 122	02 42 42.16 -54 30 42.1	162.75 152.61 0
14219+2555	RX Boo	14 24 11.627 +25 42 13.40	7.90 4.06 134	14 21 56.67 +25 55 49.0	45.69 24.84 130
16387-2700	AX Sco	16 41 49.757 -27 06 19.34	1.16 0.68 0	16 38 43.92 -27 00 37.4	56.51 43.51 0
19194+1734	T Sge	19 21 42.048 +17 39 59.81	6.24 6.06 0	19 19 28.18 +17 34 16.0	36.04 35.03 0
20079-0146	V584 Aql	20 10 29.828 -01 37 40.85	22.93 21.24 90	20 07 54.38 -01 46 35.9	92.88 92.47 90
17123+1107	V438 Oph	17 14 39.778 +11 04 09.89	0.85 0.71 0	17 12 18.82 +11 07 31.5	51.51 39.51 0
13022-7650	DL Cha	13 00 04.68 -78 28 57.7	280 90 0	12 56 09.62 -78 12 47.2	280 90 0
13303-0656	S Vir	13 33 00.108 -07 11 41.02	14.32 8.18 103	13 30 23.18 -06 56 18.0	83.73 46.23 102
13462-2807	W Hya	13 49 01.998 -28 22 03.49	10.50 6.67 110	13 46 12.18 -28 07 06.6	59.93 39.57 110
02427-5430	W Hor	02 44 14.752 -54 18 04.11	29.81 28.12 122	02 42 42.16 -54 30 42.1	162.75 152.61 0
14219+2555	RX Boo	14 24 11.627 +25 42 13.40	7.90 4.06 134	14 21 56.67 +25 55 49.0	45.69 24.84 130
16387-2700	AX Sco	16 41 49.757 -27 06 19.34	1.16 0.68 0	16 38 43.92 -27 00 37.4	56.51 43.51 0
17123+1107	V438 Oph	17 14 39.778 +11 04 09.89	0.85 0.71 0	17 12 18.82 +11 07 31.5	51.51 39.51 0
19194+1734	T Sge	19 21 42.048 +17 39 59.81	6.24 6.06 0	19 19 28.18 +17 34 16.0	36.04 35.03 0
20038-2722	V1943 Sgr	20 06 55.244 -27 13 29.76	6.23 4.22 0	20 03 51.92 -27 22 09.0	36.04 24.37 0
20079-0146	V584 Aql	20 10 29.828 -01 37 40.85	22.93 21.24 0	20 07 54.39 -01 46 35.8	55.01 54.32 0
06551+0322	AZ Mon	06 57 45.19 +03 18 09.3	290 290 86	06 55 07.67 +03 22 13.6	290 290 0
10580-1803	R Crt	11 00 33.853 -18 19 29.58	7.31 6.50 0	10 58 05.95 -18 03 22.1	42.06 37.66 0
04361-6210	R Dor	04 36 45.592 -62 04 37.76	6.77 6.09 3	04 36 10.40 -62 10 31.6	39.58 37.01 7
04265+5718	RV Cam	04 30 41.679 +57 24 42.26	6.25 6.09 147	04 26 31.86 +57 18 13.0	34.57 34.54 148
12046-0629	RW Vir	12 07 14.903 -06 45 56.07	3.52 2.55 0	12 04 41.04 -06 29 15.0	20.31 14.72 0
20502+4709	RZ Cyg	20 51 53.18 +47 21 20.4	290 290 41	20 50 12.48 +47 10 00.0	290 290 53
22035+3506	SV Peg	22 05 42.084 +35 20 54.53	10.89 10.27 90	22 03 31.02 +35 06 17.3	62.95 59.40 90
00192-2020	T Cet	00 21 46.274 -20 03 28.88	8.76 4.23 87	00 19 14.48 -20 20 06.6	51.25 25.36 86
04020-1551	V Eri	04 04 18.800 -15 51 38.9	49.22 48.25 0	04 02 01.57 -15 51 38.9	49.22 48.25 0
02469+5646	W Per	02 50 37.891 +56 59 00.25	9.17 8.92 29	02 46 55.37 +56 46 38.2	53.29 50.30 24

IRAS PSC Name	Source	Gal. Coord.			Parallax
		Longtitude	Latitude		
20038-2722	V1943 Sgr	14.7708	-27.6823	6.23 4.22 0	5.07
02427-5430	W Hor	273.4749	-55.8919	29.81 28.12 0	-
14219+2555	RX Boo	34.2774	69.2127	7.90 4.06 134	5.24
16387-2700	AX Sco	353.2753	12.5194	1.16 0.68 0	2.93
19194+1734	T Sge	52.0438	1.5316	6.24 6.06 0	1.93
20079-0146	V584 Aql	40.7312	-18.2879	22.93 21.24 89	-
17123+1107	V438 Oph	32.1306	26.4553	0.85 0.71 0	1.64
13022-7650	DL Cha	303.3796	-15.6185	280 90 0	-
13303-0656	S Vir	320.7591	54.2321	14.32 8.18 103	0.9
13462-2807	W Hya	318.0223	32.8108	10.50 6.67 110	9.59
02427-5430	W Hor	273.4749	-55.8919	29.81 28.12 0	-
14219+2555	RX Boo	34.2774	69.2127	7.90 4.06 134	5.24
16387-2700	AX Sco	353.2753	12.5194	1.16 0.68 0	2.93
17123+1107	V438 Oph	32.1306	26.4553	0.85 0.71 0	1.64
19194+1734	T Sge	52.0438	1.5316	6.24 6.06 0	1.93
20038-2722	V1943 Sgr	14.7708	-27.6823	6.23 4.22 0	5.07
20079-0146	V584 Aql	40.7312	-18.2879	22.93 21.24 0	-
06551+0322	AZ Mon	210.7095	2.909	290 290 93	-
10580-1803	R Crt	269.2695	37.1958	731 6.50 0	3.83
04361-6210	R Dor	272.6714	-39.3424	6.77 6.09 3	18.31
04265+5718	RV Cam	149.2132	6.199	6.25 6.09 147	0.82
12046-0629	RW Vir	283.8239	54.4585	3.52 2.55 0	3.69
20502+4709	RZ Cyg	87.0343	1.887	290 290 0	-
22035+3506	SV Peg	88.7152	-16.2855	10.89 10.27 90	4.28
00192-2020	T Cet	77.5149	-80.1979	8.76 4.23 87	3.7
04020-1551	V Eri	208.8489	-43.9775	8.51 8.33 0	2.28
02469+5646	W Per	138.6545	-2.2048	9.17 8.92 29	0.35

IRAS PSC Name	Source	Fluxes					
			B	V	J	H	K
20038-2722	V1943 Sgr	DCCC	9.25	-	-0.085	-1.123	-1.523
02427-5430	W Hor	DCCC	10.06	-	1.629	0.709	0.32
14219+2555	RX Boo	DCCC	9.24	-	-0.661	-1.535	-1.931
16387-2700	AX Sco	CCCCC	10.09	8.53	2.159	1.224	0.901
19194+1734	T Sge	DDCCC	11	9.32	1.585	0.429	0.093
20079-0146	V584 Aql	DCCC	10.61	-	2.136	1.147	0.801
17123+1107	V438 Oph	DCCC	10.6	-	1.871	0.935	0.551
13022-7650	DL Cha	DCCC	13.59	-	2.783	1.621	1.189
13303-0656	S Vir	ECCC	-	6.3	1.454	0.65	0.249
13462-2807	W Hya	DDD	8.86	7.5	-1.737	-	-
02427-5430	W Hor	DCCC	10.06	-	1.629	0.709	0.32
14219+2555	RX Boo	DCCC	9.24	-	-0.661	-1.535	-1.931
16387-2700	AX Sco	CCCCC	10.09	8.53	2.159	1.224	0.901
17123+1107	V438 Oph	DCCC	10.6	-	1.871	0.935	0.551
19194+1734	T Sge	DDCCC	11	9.32	1.585	0.429	0.093
20038-2722	V1943 Sgr	DDDDE	9.25	8.04	-0.085	-1.123	-1.523
20079-0146	V584 Aql	DDEDD	10.55	9.19	2.136	1.147	0.801
06551+0322	AZ Mon	EDDDD	11.7	13	3.908	2.646	2.005
10580-1803	R Crt	DDDDE	10.33	8.92	0.173	-0.896	-1.403
04361-6210	R Dor	CCCCC	6.97	5.73	-2.652	-3.732	-4.227
04265+5718	RV Cam	CCCCC	9.65	8.2	1.667	0.602	0.412
12046-0629	RW Vir	CCDDD	8.6	7.18	1.459	0.528	0.216
20502+4709	RZ Cyg	DEDDD	11.4	9.8	2.2	1.06	0.59
22035+3506	SV Peg	DCCC	10.11	-	1.106	-0.092	-0.399
00192-2020	T Cet	CCCCC	7.32	5.74	0.496	-0.482	-0.808
04020-1551	V Eri	DDDDE	9.96	8.59	0.833	-0.318	-0.749
02469+5646	W Per	CCCCC	11.6	9.11	3.095	1.999	1.568

Appendix B

Title of Appendix B goes here

In the process of analyzing the various spatial resolution spectra, we made an effort to have an autonomous analysis using IDL programming language. This would allow for a more rapid analysis and remove some notions of researcher's bias. Below is the code that was developed for this purpose. However, the output of this code was not satisfactory.

Figures B.2 and B.1 show an example of the Gaussian fit results from running the autonomous program. A Gaussian fit was used to match the one used in the IRAF analysis. Figure B.1 appears to be a good fit, but figure B.2 is appears to be a poor fit. The difficulty with creating a proper fit could not be remedied and the attempt to create an autonomous Gaussian fitting program was abandoned.

B.1 Automatic.pro

```
;;Data Analysis for Research on Spacial Resolution of the 13 Micron
    Feature
;;By: Nelson de Souza (10246799) ;;Last updated: July 18, 2012
;;The purpose of this program is to load a spectra and determine the
    peak position, equivalent width, and full width half maximum of the
     13 micron feature.

function countpoints, file, index
        ;;This function counts how many data points we have
```

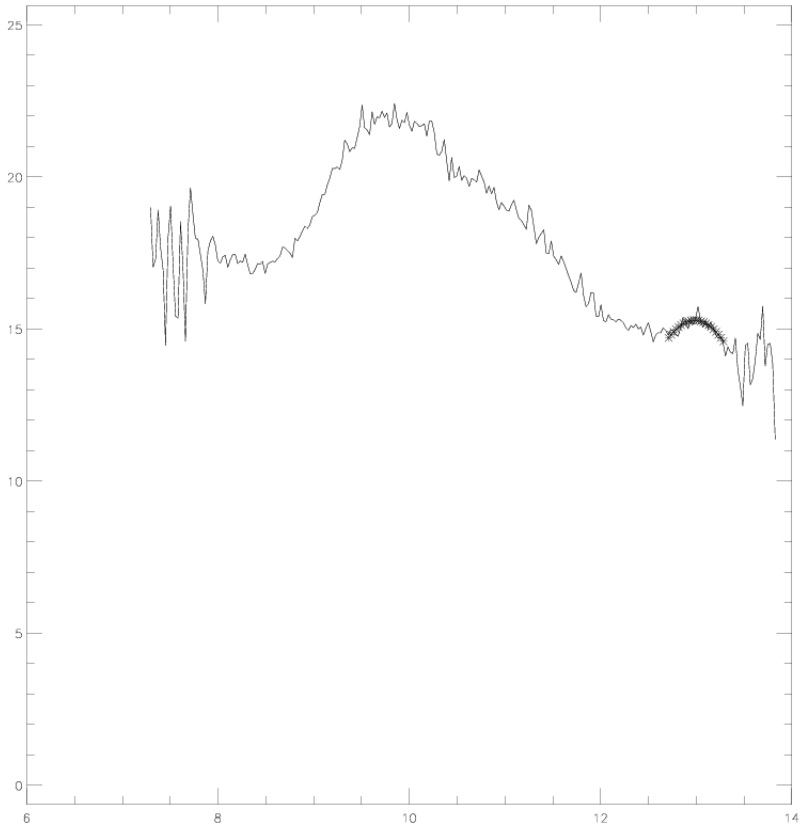

Figure B.1: An example of a good Gaussian fit using automatic.pro

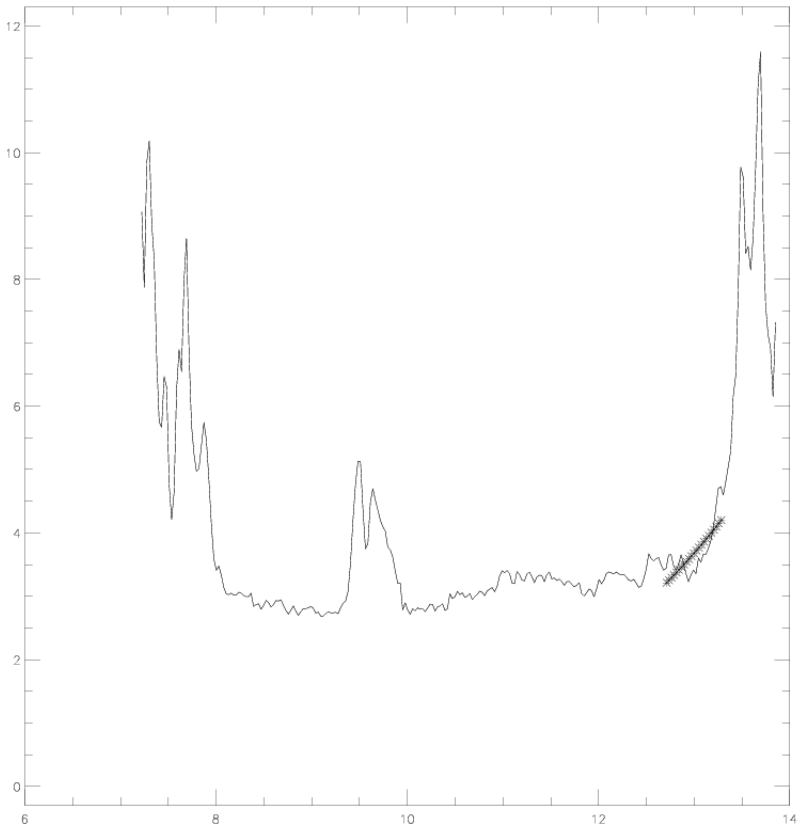

Figure B.2: An example of a bad Gaussian fit using automatic.pro.

```
        openr, 2, file
        str='' index=0
        while ~ eof(2) do begin
                readf, 2, str
                index=index+1
        endwhile
        close, 2
return, index
end

pro autoanalysis
        dir='/home/nddz7/Desktop/Summer2012/RLeo/'

        set_plot, 'ps'
        device, filename=dir+'\plot.ps', /inches, xsize=10, ysize=10, /
            portrait, xoffset=0.9, yoffset=8.5, scale_factor=0.85

        lowwav=12.7
        highwav=13.3

        numfiles=countpoints(dir+'file_names.txt') ;;Calculate the
            number of files we have
        st={magnitudes,thrtpeak:0.0,thrtfwhm:0.0,thrteqw:0.0}
        analysis=replicate(st, numfiles)
        namelist=strarr(numfiles,1)
        temp1=''
        openw, 4, '/home/nddz7/Desktop/Summer2012/RLeo/Result.txt'

        tempfile=dir+'file_names.txt'
        openr, 1, tempfile
        for i=0, numfiles-1 do begin
                readf, 1, temp1
                namelist[i]=temp1 ;;An array with the name of each file
                    in their own array cell
                ;;analysis[i].name=temp1
        endfor
        close, 1
```

```
for name=0,numfiles-1 do begin ;;Make spectra array
        file=dir+namelist[name]
        count=countpoints(file) ;;Determine how many data
            points are in the current spectra being analyzed
        fullspectra=fltarr(count,2) ;;Create a floating-point
            array of the number of data points
        openr, 3, file

        fulltri=fltarr(count,2) ;;Create a synthetic data set
            for debugging

        for i=0, count-1 do begin ;;Put the raw data into an
            array for easier access to analyze
                readf, 3, temp2, temp3
                fullspectra[i,0]=temp2
                fullspectra[i,1]=temp3

                fulltri[i,0]=temp2 ;;Generate a synthetic data
                    set for debugging
                fulltri[i,1]=(0.5*exp(-(((fulltri[i,0]-13)/2)
                    ^2)/2))+((1.0/150.0)*randomn(systime_seed))
        endfor
        close, 3

numrsp=n_elements(fullspectra[*,0]) ;;Make an array of only the
    data points we want fit. In this case the 13um.
        siz=0
        for j=0, numrsp-1 do begin
                if (fullspectra[j,0] ge lowwav) && (fullspectra
                    [j,0] le highwav) then begin
                        siz=siz+1
                endif
        endfor

trix=fltarr(siz,1) ;;Synthetic data set of only the 13micron
    area for debugging
```

```
triy=fltarr(siz,1) ;;Synthetic data set of only the 13micron
    area for debugging

thrtspectra=fltarr(siz,2)
er=fltarr(siz,1)
        index=0
        for j=0, numrsp-1 do begin
                if (fullspectra[j,0] gt lowwav) && (fullspectra
                    [j,0] lt highwav) then begin
                        thrtspectra[index,0]=fullspectra[j,0]
                        thrtspectra[index,1]=fullspectra[j,1]

                        trix[index,0]=fulltri[j,0]
                        triy[index,0]=fulltri[j,1]

                        ;ave=(fullspectra[j-2,1]+fullspectra[j
                            -1,1]+fullspectra[j,1]+fullspectra[
                            j+1,1]+fullspectra[j+2,1])/5
                        ave=(fullspectra[j-1,1]+fullspectra[j
                            ,1]+fullspectra[j+1,1])/3
                        er[index,0]=sqrt((thrtspectra[index,1]-
                            ave)*(thrtspectra[index,1]-ave))
                        index=index+1
                endif
        endfor

;estimate=fltarr(3,1)
;estimate[0,0]=3.0
;estimate[1,0]=13.0
;estimate[2,0]=2.0

estimate=[3.,13.,2.]
;fit=GAUSSFIT(trix[*,0], triy[*,0], coeff, ESTIMATES=estimate,
    NTERMS=3)
fit=GAUSSFIT(thrtspectra[*,0], thrtspectra[*,1], coeff, NTERMS
    =3) ;, MEASURE_ERRORS=er[*,0])
;analysis[name].thrtpeak=coeff[1]
```

```
;analysis[name].thrtfwhm=2*SQRT(2*ALOG(2))*coeff[2]

;print, analysis[name].thrtpeak
;print, analysis[name].thrtfwhm
print, namelist[name]

;Testing and debugging stuff
;plot, fulltri[*,0], fulltri[*,1], psym=2
;oplot,trix[*,0], triy[*,0], psym=5
;oplot, trix[*,0], fit, psym=1
print, coeff
;print, thrtspectra[*,0]

plot, fullspectra[*,0], fullspectra[*,1], ystyle=2
;plot, thrtspectra[*,0], thrtspectra[*,1], psym=5
oplot, thrtspectra[*,0], fit, psym=2

;;Calculate standard deviation and r squared
sum=0.0
expt = 0.0
z = 0.0
dsq=0.0
sstot=0.0
sserr=0.0
rsqr=0.0
ssreg=0.0
std=0.0

for n=0, index-1 do begin
        sum=sum+thrtspectra[n,1]

        z=(thrtspectra[n,0]-coeff[1])/coeff[2]
        expt=coeff[0]*exp(-(z^2)/2)
        dsq=dsq+(thrtspectra[n,1]-expt)^2
endfor
average=sum/index
std=(sqrt(dsq/(index-1)))/sqrt(index)
```

```
        for n=0, index-1 do begin
                sstot=sstot+((thrtspectra[n,1]-average)^2)
                z=(thrtspectra[n,0]-coeff[1])/coeff[2]
                expt=coeff[0]*exp(-(z^2)/2)
                ssreg=ssreg+((expt-average)^2)
                sserr=sserr+((thrtspectra[n,1]-expt)^2)
        endfor

        rsqr=1-(sserr/sstot)
        rsq=ssreg/sstot
        ;print, 'rsquard is:', rsqr
        ;print, 'other:', rsq
        ;print, 'stdev:', std

        printf, 4, rsqr, rsq, coeff, namelist[name]
        endfor

        device, /close_file
        close, 4
        fin:
        print, 'end'
end
```